



**HAL**  
open science

## **Undrained cylindrical cavity expansion/contraction in stiff clays using a two-surface plasticity model**

Wei Cheng, Ren-Peng Chen, Jean-Michel Pereira, Yu-Jun Cui

### ► **To cite this version:**

Wei Cheng, Ren-Peng Chen, Jean-Michel Pereira, Yu-Jun Cui. Undrained cylindrical cavity expansion/contraction in stiff clays using a two-surface plasticity model. *International Journal for Numerical and Analytical Methods in Geomechanics*, 2022, 46 (3), pp.570-593. <10.1002/nag.3312>. <hal-03558777>

**HAL Id: hal-03558777**

**<https://enpc.hal.science/hal-03558777v1>**

Submitted on 4 Feb 2022

**HAL** is a multi-disciplinary open access archive for the deposit and dissemination of scientific research documents, whether they are published or not. The documents may come from teaching and research institutions in France or abroad, or from public or private research centers.

L'archive ouverte pluridisciplinaire **HAL**, est destinée au dépôt et à la diffusion de documents scientifiques de niveau recherche, publiés ou non, émanant des établissements d'enseignement et de recherche français ou étrangers, des laboratoires publics ou privés.



HAL Authorization

1        **Undrained cylindrical cavity expansion/contraction in stiff**  
2                                    **clays using a two-surface plasticity model**

3                                    Wei Cheng<sup>1</sup>, Ren-peng Chen<sup>2,\*</sup>, Jean-Michel Pereira<sup>3</sup>, Yu-jun Cui<sup>4</sup>

4  
5        <sup>1</sup>*Former Ph.D student, Department of Civil Engineering, Zhejiang University, Hangzhou 310058, China,*  
6        *wcheng@zju.edu.cn*

7        <sup>2</sup>*Professor, Department of Civil Engineering, Zhejiang University, Hangzhou 310058, China; College of Civil*  
8        *Engineering, Hunan University, Changsha 410082, China; chenrp@zju.edu.cn, chenrp@hnu.edu.cn*  
9        (Corresponding author)

10        <sup>3</sup>*Professor, Laboratoire Navier (UMR 8205), Ecole des Ponts ParisTech, Univ Gustave Eiffel, CNRS, IFSTTAR,*  
11        *F-77455 Marne-la-Vallée, France*

12        <sup>4</sup>*Professor, Laboratoire Navier (UMR 8205), Ecole des Ponts ParisTech, Univ Gustave Eiffel, CNRS, IFSTTAR,*  
13        *F-77455 Marne-la-Vallée, France*

14  
15  
16  
17  
18  
19  
20  
21  
22  
23  
24  
25

26 **Abstract**

27 This paper presents a semi-analytical solution of undrained cylindrical cavity  
28 expansion/contraction problem using a two-surface plasticity model for natural stiff clays from the  
29 view point of poromechanics. The present solution reduces the classical boundary problem into a  
30 group of seven first-order ordinary differential equations via an auxiliary independent variable  $\zeta$   
31 under undrained conditions. It strictly follows the premise of constant soil mass. Meanwhile, the  
32 solution for the constant soil volume problem is used for comparison. It shows that constant soil  
33 mass assumption is of paramount importance in developing solutions under high stress condition,  
34 while constant soil volume induces non-negligible errors in effective stress and pore pressure  
35 distributions. Based on the premise of constant soil mass, extensive parametric studies on cavity  
36 expansion/contraction are undertaken to investigate the effects of the model key parameters on the  
37 stress components distribution, excess pore pressure distribution and cavity expansion curves. The  
38 present solution could be useful while dealing with geotechnical and petroleum engineering  
39 problems involving stiff clays or soft claystones. The application in Praclay Gallery excavation in  
40 natural Boom clay well demonstrates the validity of the present solution.

41 **Keywords:** stiff clays; cavity expansion/contraction; undrained condition; constant soil mass;  
42 elastoplasticity; poromechanics

43

44

45

46

47

48

49

50

51

52

53

54

55 **1. Introduction**

56 Cavity expansion theory has been widely applied to interpreting the results from some in situ tests  
57 such as cone penetration and pressuremeter tests, analyzing the stresses and deformations induced  
58 by wellbore drilling, gallery excavation, tunneling and pile installation. Over the past decades,  
59 various analytical and semi-analytical solutions [1-13] for cylindrical and spherical cavity  
60 expansions have been developed. With the increasing complexity of constitutive models, from  
61 elastic models, elastic perfectly plastic models to critical state models, the solutions are  
62 increasingly realistic. Among these models, original and modified Cam-clay models have gained  
63 large popularity in solving the cavity expansion and contraction problems for their capability of  
64 modelling strain hardening/softening behaviors of soils. Carter et al. [14] firstly investigated the  
65 cavity expansion problems with original Cam-clay model by means of finite element analysis.  
66 Collins and Yu [6] developed a general solution for large strain undrained cavity expansion using  
67 both original and modified Cam-clay models with and without zero initial radius assumption. Cao  
68 et al. [7], by following Collins and Yu's approach, developed a semi-analytical solution for  
69 undrained cavity using modified Cam-clay model. Mo and Yu [8], extended the original Cam-clay  
70 model to a unified state parameter model for clays and sands, then developed a novel solution for  
71 both cylindrical and spherical cavity problems. Russell and Khalili [29], using the similarity  
72 technique, investigated the cavity expansion problem in unsaturated soils by a unified bounding  
73 surface model to consider the influence of suction and moisture content. That study demonstrated  
74 there was no difficulty in solving cavity expansion problems using two-surface constitutive  
75 models. However, it should be noted that the initial stress state is assumed isotropic and the  
76 vertical stress is omitted in two stress invariants in that similarity approach [6]. Recently, Chen  
77 and Abousleiman [9-11] proposed novel semi-analytical solutions for both drained and undrained  
78 cylindrical cavity expansion/contraction problems. Their solutions removed the limitation on the  
79 initial condition of isotropic stress state and depicted a more general case of in situ situation by  
80 considering the vertical stress around the expanded/contracted cavity. Based on this versatile  
81 framework, Chen et al. [12] used the semi-analytical solution to analyze the three-dimensional  
82 strength and the anisotropic properties of soils by introducing Spatially Mobilized Plane (SMP)  
83 criterion in modified Cam-clay model. More recently, fabric and stress induced anisotropy has

84 also been accounted for using anisotropic elastoplastic models like S-CLAY1 [13] and Dafalias'  
85 anisotropic bounding surface model [14]. Although various types of solutions have been proposed,  
86 most of them basically treat soil as an original or modified Cam-clay material with an associated  
87 flow rule, providing quite low accuracy in modelling heavily over-consolidated clays. In particular,  
88 for highly plastic stiff clays or soft claystone, high clay contents, low void ratios, low permeability  
89 and high stress states (usually greater than 1 MPa) distinguish them from Cam-clay materials with  
90 the following basic hydro-mechanical behaviors:

91 (1) Highly nonlinear behaviors are typically observed on stiff clays at heavily over-consolidated  
92 states [16]. These pre-yielding nonlinear behaviors would have significant influence on the  
93 variations of pore pressure and displacements which are described by advanced constitutive  
94 modelling for stiff clays [16, 17, 18, 22].

95 (2) For highly plastic stiff clays, the yield surface is of a 'tear' shape rather than an 'elliptical'  
96 shape. An 'elliptical' shape would overestimate the failure stress on the 'dry side' but  
97 underestimate it on the 'wet side'. The yield surface shape variation would lead to misestimating  
98 the excess pore pressure under undrained conditions. On the other hand, the plastic flow direction  
99 should also be considered for the complex behavior of stiff clays.

100 (3) The pore fluid governs the distribution of excess pore pressure and stress components in  
101 expanding process. In relatively low stress states (e.g. 0.1 MPa~1 MPa) under undrained  
102 conditions, the volumetric strain due to loading remains almost constant. However, for stiff clays  
103 and soft claystone at great depth (e.g. 1MPa~100MPa), the pore water would induce a slight  
104 volumetric strain itself, which can significantly influence the excess pore pressure.

105 These three main differences make the existing analytical solutions [6-14] difficult to be used  
106 directly in analyzing tunneling and piezocone penetration tests in stiff clays under deep ground.  
107 On the other hand, although several two-surface plasticity (bounding/subloading surface) models  
108 have already been numerically applied into tunnel/gallery construction, e.g. the ground movement  
109 (settlement or uplift) induced by tunneling in stiff London clay[38-39] or Shanghai soft clay[37],  
110 the excess pore water pressure distribution in Boom clay[35], the characteristic of load transfer in  
111 shanghai clay during tunnel operating period[36], the corresponding novel analytical or  
112 semi-analytical solutions are still appealing. Based on the rigorous semi-analytical framework  
113 proposed by Chen and Abousleiman [9] and the premise of constant soil mass, the study extends

114 the solution with a two-surface plasticity model named ACC2 [16] to consider the mechanical  
 115 behavior of natural stiff clays under high stress conditions. After a brief introduction of the basic  
 116 formulas, the main features and parameters of the two-surface plasticity model, it is extended to  
 117 undrained conditions by incorporating the mass conservation for the liquid phase in the pore space.  
 118 By using the incremental stress-strain relationship, the undrained cavity expansion/contraction  
 119 problem is formulated to solve a system of first-order ordinary differential equations with two  
 120 different premises, namely constant soil volume and constant soil mass, respectively. A discussion  
 121 between Constant Soil Volume (CSV) and Constant Soil Mass (CSM) assumptions is included to  
 122 highlight that undrained condition corresponds to a situation with constant soil mass. Further  
 123 parametric studies based on four key material parameters about stress paths, stress distribution and  
 124 cavity expansion/contraction curves are conducted. Lastly, as a precise and convenient tool, the  
 125 present semi-analytical solution is utilized to predict the pore pressure and stress distribution along  
 126 the radial distance and the supporting pressure which is required to maintain the Gallery stability  
 127 in the case of Praclay Gallery in underground research facility HADES-URF built at a depth of  
 128 223m in natural Boom clay.

129

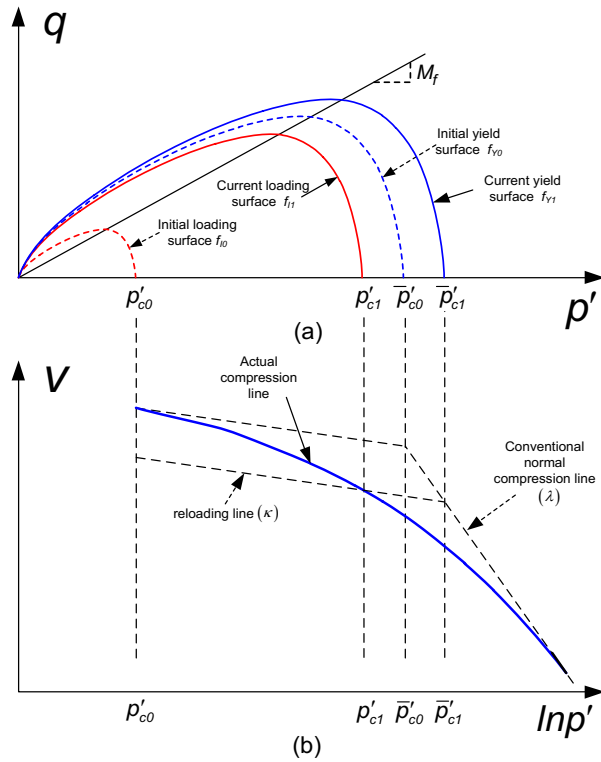
## 130 **2. Model description**

131 This section gives a brief description of the two-surface plasticity model for stiff clays (e.g.  
 132 natural Boom clay) named ACC2 [16]. The formulation of ACC2 model is based on the triaxial  
 133 conditions with three principal stresses (namely,  $\sigma'_r$ ,  $\sigma'_\theta$ ,  $\sigma'_z$  in a cylindrical coordinate  
 134 system):

$$135 \quad p' = \frac{1}{3}(\sigma'_r + \sigma'_\theta + \sigma'_z) \quad (1)$$

$$136 \quad q = \sqrt{\frac{1}{2}((\sigma'_r - \sigma'_\theta)^2 + (\sigma'_r - \sigma'_z)^2 + (\sigma'_\theta - \sigma'_z)^2)} \quad (2)$$

137



138 Fig.1 Schematic plot of two surface plasticity model ACC2: (a)  $p'$ - $q$  plane; (b)  $v$ - $\ln p'$  plane

139 Fig.1 gives a schematic illustration of the two surfaces (Loading surface and Yield surface).  
 140 These two surfaces are linked through a progressive hardening relationship by a positive scalar  $r$   
 141 in  $v$ - $\ln p'$  plane. A smooth compression behavior is achieved via the use of two hardening variables  
 142  $\bar{p}'_c$  and  $r$  before the soil reaches normally consolidated states:

$$143 \quad r = \frac{p'}{\bar{p}'} = \frac{q}{\bar{q}} = \frac{p'_c}{\bar{p}'_c} \quad (3)$$

144 where  $p'_c$  is the actual loading yield stress on the Loading surface and  $\bar{p}'_c$  is the conventional  
 145 pre-consolidation pressure on the conventional Normal Compression Line.

146 Similar to the concept of bounding surface plasticity, the current stress point ( $p'$ ,  $q$ ) is  
 147 assumed to always lie on the Loading surface which is expressed as:

$$148 \quad f_l(p', q, r, p'_c) = q^2 + \frac{M_f^2}{1 - k_f} \left( \frac{p'}{r\bar{p}'_c} \right)^{k_f} (r\bar{p}'_c)^2 - \frac{M_f^2 p'^2}{1 - k_f} = 0 \quad (4)$$

149 where  $M_f$  is the stress ratio at the apex of the two surfaces and  $k_f$  is a parameter specifying the  
 150 shape of the yield surfaces. Because natural stiff clays (e.g. natural Boom clay) show a unique  
 151 yielding behavior, a generalized yield surface ( $k_f < 2$ ) is adopted in this model. While  $k_f$  varies

152 from 0.5 to 2, a tear shape surface turns into an elliptical shape more suitable to soft clays in Fig.  
 153 2(a). The calibrated yielding behavior of natural Boom clay shows that the closest value of  $k_f$  is  
 154 0.7.

155 Two internal variables, namely  $\bar{p}'_c$  and  $r$ , are used to control the plastic strain hardening or  
 156 softening behavior. A cam-clay type volumetric plastic strain isotropic hardening law for  $d\bar{p}'_c$  is  
 157 adopted:

$$158 \quad d\bar{p}'_c = \frac{v}{\lambda - \kappa} \bar{p}'_c d\varepsilon_v^p \quad (5)$$

159 where  $v$  is the specific volume;  $\lambda$  is the slope of conventional normal compression line in  $v$ - $\ln p'$   
 160 plane;  $\kappa$  is the slope of reloading line in  $v$ - $\ln p'$  plane;  $d\varepsilon_v^p$  is the volumetric plastic strain  
 161 increment.

162 Meanwhile, a progressive hardening law for  $dr$  is introduced with a generalized plastic strain  
 163 to account for the contribution of both volumetric and shear plastic deformation parts. It should be  
 164 noted that different strain types are considered in previous works [30, 31, 32]. Russell and Muir  
 165 Wood [28] pointed out that the inclusion of both volumetric and shear parts was of paramount  
 166 importance in accurately describing soil behavior. This hardening law reads as follows:

$$167 \quad dr = \frac{v}{\lambda - \kappa} s(1-r) d\varepsilon_d^p = \frac{v}{\lambda - \kappa} s(1-r) (d\varepsilon_v^p + A_d d\varepsilon_s^p) \quad (6)$$

168 where  $s$  is the key material parameter ( $s > 0$ ) that determines the rate at which the Loading surface  
 169 hardens towards the Yield surface;  $A_d$  is a material parameter ( $A_d > 0$ ) which controls the  
 170 contribution of plastic shear strain to strain hardening.

171 As plotted in Fig.2(c),  $s$  controls the nonlinearity of the isotropic compression line in  
 172 over-consolidated states in  $v$ - $\ln p'$  plane. As  $s$  varies from 4 to 1000, the behavior switches from a  
 173 nonlinear trend to a bi-loglinear behavior as in the modified cam-clay model. Calibrated with the  
 174 test results of natural Boom clay, a value of 8 is found for  $s$ .

175 As plotted in Fig.2(d), parameter  $A_d$  ( $A_d \geq 0$ ) can be obtained by fitting stress paths during  
 176 drained softening stages in highly over-consolidated states. Parameter  $A_d$  describes how the plastic  
 177 shear strain affects the hardening process. As  $A_d$  varies from 0 to 5, the nonlinearity on the 'dry  
 178 side' is increasingly obvious. It is noteworthy that when  $A_d = 0$ , the plastic shear strain does not  
 179 contribute to the hardening process anymore. The most suitable value of  $A_d$  for natural Boom clay

180 is 0.1.

181 The stress dilatancy relation proposed by McDowell et al. [19] is adopted to define a  
 182 non-associated flow rule for better describing the volumetric strain and excess pore pressure  
 183 generation during undrained loadings for natural stiff clays. Assuming a plastic potential having  
 184 the same shape as the yield surfaces but a different pair of parameters ( $M_g, k_g$ ), the stress dilatancy  
 185 equation and the non-associated flow rule are expressed as follows:

$$186 \frac{d\varepsilon_v^p}{d\varepsilon_s^p} = \frac{\frac{\partial g_l}{\partial p}}{\frac{\partial g_l}{\partial q}} = \frac{M_g^2 - \eta^2}{k_g \eta} \quad (7)$$

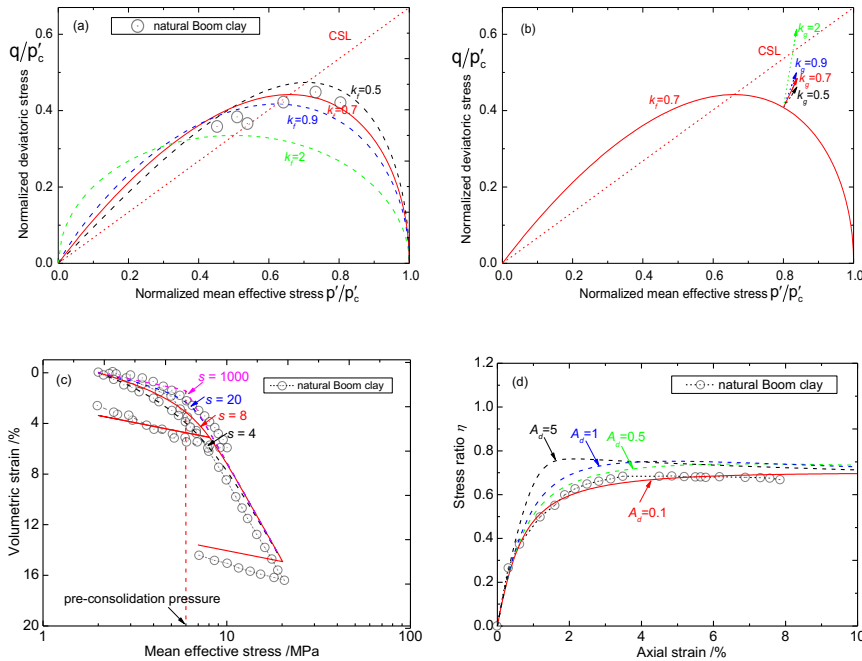
$$187 d\varepsilon_v^p = \Lambda \frac{\partial g_l}{\partial p}, \quad d\varepsilon_s^p = \Lambda \frac{\partial g_l}{\partial q} \quad (8)$$

188 where  $\eta$  denotes the stress ratio  $q/p'$ ,  $M_g$  is the critical state ratio where no further volumetric  
 189 strain develops and  $k_g$  controls the shape of the plastic potential and the direction of plastic flow.

190 Fig.2(b) depicts the variation of plastic flow direction ( $k_g$ ) from 0.5 to 2 in  $p'$ - $q$  plane. The  
 191 calibrated yielding behavior of natural Boom clay shows that the closest value of  $k_g$  is 0.9.

192

193



194

195 Fig.2 Variation of parameters of ACC2 model in  $p'$ - $q$  plane and  $v$ - $\ln p'$  plane: (a)  $k_f$  varies from 0.5

196 to 2; (b)  $k_g$  varies from 0.5 to 2; (c)  $s$  varies from 4 to 1000; (d)  $A_d$  varies from 0.1 to 5

197 With eleven material parameters (five of them are the same as MCC model), the two-surface  
 198 plasticity model named ACC2, similarly to bounding surface plasticity theory, has been proposed  
 199 to consider the mechanical behavior of both normally consolidated and over-consolidated stiff  
 200 clays. Five of them ( $\lambda$ ,  $\kappa$ ,  $\bar{p}'_c$ ,  $\nu$ ,  $M_f$ ) are the same as for the modified cam-clay model.  $r$  denotes  
 201 the inverse of over-consolidation ratio. Two parameters ( $k_f$ ,  $k_g$ ) control the shapes of the yield  
 202 surface and the plastic potential surface. Two parameters ( $s$ ,  $A_d$ ) are used to account for a  
 203 progressive hardening mechanism in over-consolidated states. Thus, the following discussion  
 204 about ACC2 model is mainly done by considering four principal parameters, namely  $k_f$  (shape of  
 205 yield surface),  $k_g$  (direction of plastic flow),  $s$  (isotropic compression nonlinearity) and  $A_d$   
 206 (deviatoric nonlinearity).

207

### 208 **3. Problem statement**

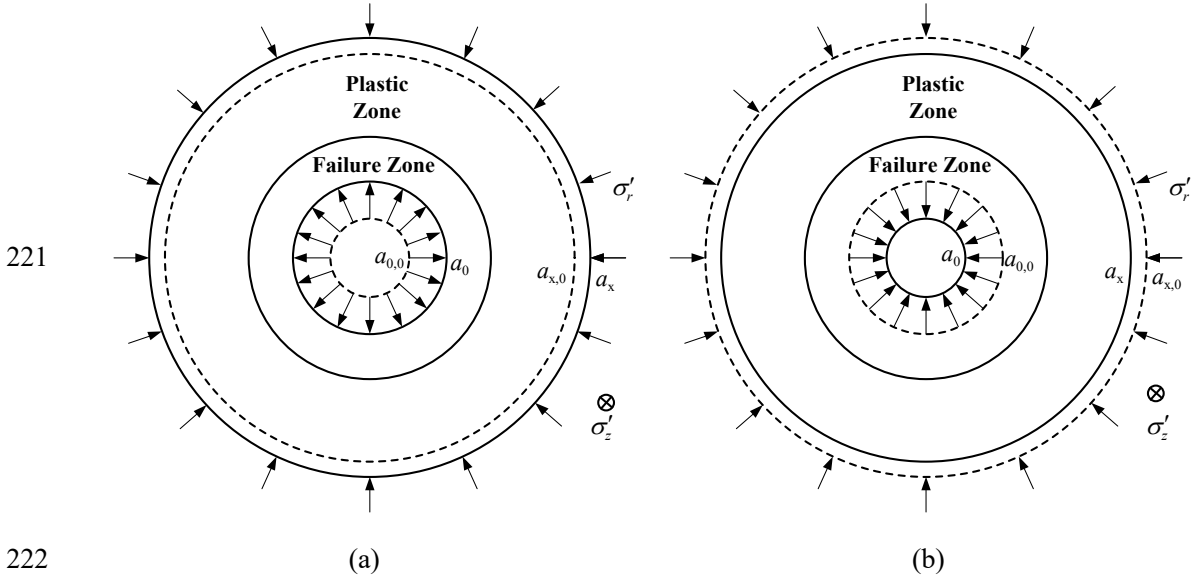
#### 209 **3.1 Undrained cylindrical cavity expansion/contraction**

210 Fig.3 presents schematic plots of cylindrical cavity expansion/contraction problems with initial  
 211 radius  $a_{0,0}$  in an infinite elasto-plastic soil layer under undrained conditions. As the cavity expands  
 212 or shrinks from initial radius  $a_{0,0}$  to current radius  $a_0$ , a failure zone would be formed in the  
 213 vicinity of the cavity wall. At the same time, the outside zone limited by radius  $a_{x,0}$  would be  
 214 plastic with stress points always lying on the Loading surface. Beyond that radius, the soil is in the  
 215 elastic regime.

216 The radial equilibrium equation for cylindrical cavity expansion/contraction problem is  
 217 expressed in terms of the effective stress as:

$$218 \quad \frac{d\sigma'_r}{da_x} + \frac{\sigma'_r - \sigma'_\theta}{a_x} + \frac{du_w}{da_x} = 0 \quad (9)$$

219 where  $\sigma'_r$ ,  $\sigma'_\theta$  are radial, tangential effective stress of any material point, respectively.  $u_w$  stands  
 220 for pore pressure.



223 Fig.3 Geometry of cylindrical cavity problem: (a) expansion; (b) contraction

224 Based on the compatibility condition and large deformation theory, a generalized logarithmic  
 225 definition of strains in Eulerian description can be adopted in all areas [6]:

226 
$$\varepsilon_r = -\ln\left(\frac{da_x}{da_{x0}}\right), \quad \varepsilon_\theta = -\ln\left(\frac{a_x}{a_{x0}}\right), \quad \varepsilon_v = -\ln\left(\frac{v}{v_0}\right) \quad (10)$$

227 where  $a_x, a_{x0}$  are the current and initial radii of any material points, respectively.  $\varepsilon_r, \varepsilon_\theta, \varepsilon_v$  are the  
 228 radial, tangential and volumetric strains, respectively.  $v, v_0$  are the current and initial void ratios,  
 229 respectively.

230 For further study, they can also be expressed in incremental form, as follows:

231 
$$d\varepsilon_r = -\frac{\partial(da_x)}{\partial a_x}, \quad d\varepsilon_\theta = -\frac{da_x}{a_x}, \quad d\varepsilon_v = -\frac{dv}{v} \quad (11)$$

### 233 3.2 Elastoplastic analysis under undrained condition

234 The incremental stress-strain relationship for ACC-2 model is expressed in Lagrangian description  
 235 (see A-17 in Appendix A):

236 
$$\begin{bmatrix} D\sigma'_r \\ D\sigma'_\theta \\ D\sigma'_z \end{bmatrix} = \begin{bmatrix} c_{rr} & c_{r\theta} & c_{rz} \\ c_{\theta r} & c_{\theta\theta} & c_{\theta z} \\ c_{zr} & c_{z\theta} & c_{zz} \end{bmatrix} \begin{bmatrix} D\varepsilon_r \\ D\varepsilon_\theta \\ D\varepsilon_z \end{bmatrix} \quad (12)$$

237 where  $D$  denotes the differential of material points in Lagrangian description which should be  
 238 distinguished from  $d$  in Eulerian form.

239 Under relatively low stress and undrained conditions, most analytical and semi-analytical  
240 solutions, including Chen and Abouseleiman's method [9], consider the soil mixture as an  
241 incompressible material with the undrained Poisson's ratio being equal to 0.5 and the volumetric  
242 strain remaining constant. The volume change of pore water due to external loading is ignored.  
243 This is the case referred to as constant soil volume (CSV). Most reasonable analytical and  
244 semi-analytical solutions for undrained cavity problems are extensively developed and applied for  
245 various geotechnical problems based on this premise [6-9, 11-15]. Appendix B depicts the  
246 undrained solution in the form of five first-order ordinary differential equations for the  
247 comparative study. However, under high stress and low porosity conditions, the real  
248 compressibility of pore fluids (e. g water, oil) would exhibit a significant influence on the excess  
249 pore pressure and stress distribution along the cavity. This condition of constant soil volume can  
250 actually be relaxed by considering that undrained conditions correspond to a situation with  
251 constant soil mass (CSM).

252 The well-known Skempton coefficient  $B$ , which indicates the ratio between the change in  
253 pore pressure and the change in total applied stress in Appendix C-12, could also be used to  
254 illustrate the difference. For CSV premise, the value of  $B$  is always 1 in saturated conditions. This  
255 situation may be reasonable for soft clayey soils under low stress conditions ( $B > 0.95$ ), but not for  
256 stiff clays and soft claystone under high stress conditions (e.g.  $B \approx 0.92$  for natural Boom clay [23],  
257  $B \approx 0.75$  to  $0.84$  for Callovo–Oxfordian claystone [24, 34],  $B \approx 0.88$  for Opalinus argillite [25]). In  
258 such cases, the CSV assumption would lead to unavoidable computational errors for stress and  
259 pore pressure distributions, since the effect of pore fluids' compressibility under high stress  
260 conditions is not accounted for. Note that the compressibility of the solid particles is still  
261 neglected, since it leads to volume changes that are one order of magnitude (at least) lower than  
262 the compressibility of the pore fluid.

263

### 264 **3.3 Undrained cavity expansion/contraction seen as constant soil mass conditions**

265 In the framework of poro-elasto-plasticity theory, pore fluid is typically regarded as a  
266 compressible elastic medium with a large bulk modulus (e.g.  $2.2 \times 10^3$  MPa for water,  $1.6 \times 10^3$  MPa  
267 for oil at room temperature  $20^\circ\text{C}$  and isotropic pressure 1 MPa), which is slightly sensitive to

268 temperature and pressure variations [21]. The bulk modulus of pore fluid is usually dozens of  
 269 times that of solid grain. For most clays, the compressibility of solid grains can be neglected (e.g.  
 270  $C_s=2.0 \times 10^{-5}$  MPa<sup>-1</sup> for Illite [33], to be compared to the water compressibility  $C_w=45.5 \times 10^{-5}$   
 271 MPa<sup>-1</sup> for water). Considering infinitesimal transformation and undrained conditions (CSM), and  
 272 neglecting solid grains compressibility, pore water pressure change and soil volumetric change are  
 273 related using Eulerian porosity  $n$  and pore fluid's bulk modulus  $k_w$  ( $k_w=1/C_w$ ) as follows:

$$274 \quad du_w = \frac{d\varepsilon_v - C_s dp}{\phi(C_w - C_s)} \approx \frac{d\varepsilon_v}{nC_w} = \frac{k_w d\varepsilon_v}{n} \quad (13)$$

275 It is noteworthy that Eq (13) is deduced in the framework of poromechanics by Coussy [20].  
 276 More details are presented in Appendix C.

277 In analyses considering CSM, the soil volumetric strain increment at any material point  
 278 cannot be ignored even under undrained condition. Meanwhile, the vertical strain increment is still  
 279 null in cylindrical cavity analysis (plane strain conditions). The general incremental solution for  
 280 cylindrical cavity problem is expressed in Lagrangian description, as follows:

$$281 \quad D\varepsilon_v = -\frac{D\nu}{\nu}, \quad D\varepsilon_\theta = -\frac{Da_x}{a_x}, \quad D\varepsilon_z = 0 \quad (14)$$

282 An auxiliary independent variable  $\xi$  is chosen as the ratio of initial radial position to current  
 283 radial position for each specific particle. The following differentiations can be done:

$$284 \quad \xi = \frac{a_{x0}}{a_x}, \quad \frac{D\xi}{Da_x} = -\frac{a_{x0}}{a_x^2}, \quad \frac{D\varepsilon_\theta}{D\xi} = -\frac{Da_x}{a_x D\xi} = \frac{a_x}{a_{x0}} = \frac{1}{\xi} \quad (15)$$

285 Substituting Eq (15) into Eq (12), the incremental stress-strain relationship can be  
 286 transformed into three first-order ordinary differential equations with an unknown

287 Lagrangian-form differential  $\frac{D\varepsilon_v}{D\xi}$ :

$$288 \quad \frac{D\sigma'_r}{D\xi} = c_{rr} \frac{D\varepsilon_v}{D\xi} + \frac{c_{r\theta} - c_{rr}}{\xi} \quad (16)$$

$$289 \quad \frac{D\sigma'_\theta}{D\xi} = c_{\theta r} \frac{D\varepsilon_v}{D\xi} + \frac{c_{\theta\theta} - c_{\theta r}}{\xi} \quad (17)$$

$$290 \quad \frac{D\sigma'_z}{D\xi} = c_{zr} \frac{D\varepsilon_v}{D\xi} + \frac{c_{z\theta} - c_{zr}}{\xi} \quad (18)$$

291 At the same time, the excess pore water pressure can be given in Lagrangian description:

292 
$$Du_w = \frac{k_w}{n} D\varepsilon_v \quad (19)$$

293 Thus:

294 
$$\frac{Du_w}{D\xi} = \frac{\nu k_w}{\nu-1} \frac{D\varepsilon_v}{D\xi} \quad (20)$$

295 where  $k_w$  is the bulk modulus of pore water,  $n$  is the current porosity and  $\nu$  is current specific  
296 volume.

297 In order to make the problem solvable, let us consider  $\frac{D\varepsilon_v}{D\xi} = f$ . Substitute Eq (16) and Eq  
298 (20) into the radial equilibrium equation (9) gives:

299 
$$\left( \frac{D\sigma'_r}{D\xi} + \frac{Du_w}{D\xi} \right) \frac{d\xi}{da_x} + \frac{\sigma'_r - \sigma'_\theta}{a_x} = 0 \quad (21)$$

300 Unlike  $\frac{D\xi}{Da_x}$  in Eq (15),  $\frac{d\xi}{da_x}$  corresponds to a Eulerian description:

301 
$$\frac{d\xi}{da_x} = \frac{\frac{da_{x0}}{da_x} a_x - a_{x0}}{a_x^2} = \frac{1}{a_x} \left( \frac{da_{x0}}{da_x} - \xi \right) = \frac{1}{a_x} \left( e^{\varepsilon_r} - \xi \right) \quad (22)$$

302 Integrating Eq (10), the full form of radial strain can be obtained:

303 
$$\varepsilon_r = \varepsilon_v - \varepsilon_\theta = -\ln\left(\frac{\nu}{\nu_0}\right) + \ln\left(\frac{a_x}{a_{x0}}\right) = \ln\left(\frac{\nu_0}{\nu\xi}\right) \quad (23)$$

304 Then:

305 
$$\frac{d\xi}{da_x} = \frac{1}{a_x} \left( \frac{\nu_0}{\nu\xi} - \xi \right) \quad (24)$$

306 Making full use of Eq (16), Eq (20) and Eq (24), the radial equilibrium equation (9) turns into  
307 Eq (25):

308 
$$\left( c_{rr} f + (c_{r\theta} - c_{rr}) \frac{1}{\xi} + \frac{\nu k_w}{\nu-1} f \right) \times \frac{1}{a_x} \left( \frac{\nu_0}{\nu\xi} - \xi \right) + \frac{\sigma'_r - \sigma'_\theta}{a_x} = 0 \quad (25)$$

309 Then, an equation relating  $f$  to the other principal variables  $\sigma'_r$ ,  $\sigma'_\theta$ ,  $c_{r\theta}$ ,  $c_{rr}$ ,  $\nu$  and  $\xi$  is  
310 obtained:

$$311 \quad f = -\frac{\xi(\sigma'_r - \sigma'_\theta) + \left(\frac{\nu_0}{\nu\xi} - \xi\right)(c_{r\theta} - c_{rr})}{\left(\frac{\nu_0}{\nu} - \xi^2\right)\left(c_{rr} + \frac{\nu k_w}{\nu - 1}\right)} \quad (26)$$

312 The previous four first-order ordinary differential equations are finally reduced into a full  
313 explicit form with respect to the auxiliary independent variable  $\xi$ :

$$314 \quad \frac{D\sigma'_r}{D\xi} = c_{rr}f + \frac{c_{r\theta} - c_{rr}}{\xi} \quad (27)$$

$$315 \quad \frac{D\sigma'_\theta}{D\xi} = c_{\theta r}f + \frac{c_{\theta\theta} - c_{\theta r}}{\xi} \quad (28)$$

$$316 \quad \frac{D\sigma'_z}{D\xi} = c_{zr}f + \frac{c_{z\theta} - c_{zr}}{\xi} \quad (29)$$

$$317 \quad \frac{Du_w}{D\xi} = \frac{\nu k_w}{\nu - 1} f \quad (30)$$

318 The other three variables, namely specific volume  $\nu$ , pre-consolidation pressure  $\bar{p}'_c$  and  
319 positive scalar  $r$  are also included in the differential equations through equation (26):

$$320 \quad \frac{D\nu}{D\xi} = -\nu f \quad (31)$$

$$321 \quad \frac{D\varepsilon_v^p}{D\xi} = \frac{D\varepsilon_v}{D\xi} - \frac{D\varepsilon_v^e}{D\xi} = f - \frac{\kappa}{\nu(\sigma'_r + \sigma'_\theta + \sigma'_z)} \left( \frac{D\sigma'_r}{D\xi} + \frac{D\sigma'_\theta}{D\xi} + \frac{D\sigma'_z}{D\xi} \right) \quad (32)$$

$$322 \quad \frac{D\varepsilon_s^p}{D\xi} = \frac{D\varepsilon_s^p}{D\varepsilon_v^p} \frac{D\varepsilon_v^p}{D\xi} = \frac{k_g \eta}{M_g^2 - \eta^2} \left[ f - \frac{\kappa}{\nu(\sigma'_r + \sigma'_\theta + \sigma'_z)} \left( \frac{D\sigma'_r}{D\xi} + \frac{D\sigma'_\theta}{D\xi} + \frac{D\sigma'_z}{D\xi} \right) \right] \quad (33)$$

$$323 \quad \frac{D\bar{p}'_c}{D\xi} = \frac{\nu}{\lambda - \kappa} \bar{p}'_c \frac{D\varepsilon_v^p}{D\xi} = \frac{\nu}{\lambda - \kappa} \bar{p}'_c \left[ f - \frac{\kappa}{\nu(\sigma'_r + \sigma'_\theta + \sigma'_z)} \left( (c_{rr} + c_{\theta r} + c_{zr}) \left( f - \frac{1}{\xi} \right) + \frac{c_{r\theta} + c_{\theta\theta} + c_{z\theta}}{\xi} \right) \right] \quad (34)$$

$$324 \quad \begin{aligned} \frac{Dr}{D\xi} &= \frac{\nu}{\lambda - \kappa} s(1-r) \left( \frac{D\varepsilon_v^p}{D\xi} + A_d \frac{D\varepsilon_s^p}{D\xi} \right) \\ &= \frac{\nu}{\lambda - \kappa} s(1-r) \left[ 1 + A_d \frac{k_g \eta}{M_g^2 - \eta^2} \right] \left[ f - \frac{\kappa}{\nu(\sigma'_r + \sigma'_\theta + \sigma'_z)} \left( (c_{rr} + c_{\theta r} + c_{zr}) \left( f - \frac{1}{\xi} \right) + \frac{c_{r\theta} + c_{\theta\theta} + c_{z\theta}}{\xi} \right) \right] \end{aligned} \quad (35)$$

325 At this stage, based on the premise of CSM, the cylindrical cavity expansion/contraction  
326 problem under undrained conditions is finally reduced to seven ordinary differential equations (Eq  
327 (27), Eq (28), Eq (29), Eq (30), Eq (31), Eq (34), Eq (35)). These equations can be solved as an

328 initial boundary value problem with  $\xi$  starting from 1. It is worth noting that these ordinary  
 329 differential equations which are expressed in terms of  $\xi$  should finally be converted to the radius  
 330 position  $a_x$ . From equation (24), it is obtained:

$$331 \quad \frac{da_x}{a_x} = \frac{d\xi}{\frac{\nu_0}{\nu\xi} - \xi} \quad (36)$$

332 Integrating the above equation, the following formula is obtained:

$$333 \quad \frac{a_x}{a_0} = \exp\left(\int_{\xi(a_0)}^{\xi} \frac{d\xi}{\frac{\nu_0}{\nu\xi} - \xi}\right) \quad (37)$$

334

### 335 3.4 Initial condition

336 The classical undrained cylindrical cavity expansion/contraction problem is eventually solved  
 337 using these seven first-order ordinary differential equations with the corresponding initial stress  
 338 conditions. These stress conditions are initially defined as:

$$339 \quad \sigma'_r(a_{x0}) = \sigma'_{r0}, \quad \sigma'_\theta(a_{x0}) = \sigma'_{\theta0}, \quad \sigma'_z(a_{x0}) = \sigma'_{z0}, \quad u_w(a_{x0}) = u_{w0}, \quad \nu(a_{x0}) = \nu_0, \quad p'_c(a_{x0}) = p'_{c0},$$

$$340 \quad r(a_{x0}) = r_0$$

## 341 4. Results and discussion

342 In this section, the results obtained from the semi-analytical solution are presented for the  
 343 cylindrical cavity expansion/contraction in soils under undrained conditions. The original 11  
 344 material parameters of ACC2 model are calibrated and chosen by fitting the laboratory test  
 345 (isotropic compression, drained triaxial compression) results for natural Boom Clay according to  
 346 Hong et al. [16] (Table 1 and Table 2):  $\nu_s$  (void ratio in critical state at isotropic stress of 1 MPa) =  
 347 1.84,  $\lambda$  (slope of normal consolidation line in  $v$ - $\ln p'$  plane) = 0.18,  $\kappa$  (slope of unloading line in  
 348  $v$ - $\ln p'$  plane) = 0.02,  $M_g$  (critical state ratio) = 0.67,  $M_f$  (stress ratio at apex of yield surface) = 0.67,  
 349  $\bar{p}'_c$  (pre-consolidated pressure) = 6 MPa. The Poisson ratio  $\nu$  is assumed to be 0.3. It should be  
 350 noted that the calibration process could be improved by an appropriate genetic algorithm which  
 351 has been studied in previous literatures [40-45].

352 The undrained shear strength  $s_u$  is calculated based on the premise of constant soil volume (Wood,  
353 1990):

$$354 \quad s_u = \frac{1}{\sqrt{3}} M_g e^{(v_s - v_0)/\lambda} \quad (38)$$

355 As mentioned previously, under undrained loading process, the soil sample at low void ratio  
356 and under high stress would also induce a slight volumetric strain increment which explains the  
357 variation of pore pressure. The  $s_u$  assumed here is only for the nondimensionalization purpose.

358 This section firstly highlights the effect of the compressibility of pore fluid and the  
359 importance of solving the cavity expansion problem using poro-elasto-plasticity under various  
360 stress conditions. Representative comparisons are given in Fig. 4-6 between the results for  
361 normally consolidated soils based on constant soil volume (CSV) and constant soil mass (CSM)  
362 conditions at isotropic effective stresses of 2 MPa, 10 MPa, 50 MPa, respectively. The soil mass is  
363 fully saturated with pore water. Moreover, a full range of isotropic stresses from 0.1 MPa to 100  
364 MPa is considered to assess the relative errors between these two assumptions under cavity  
365 expansion condition ( $a_0/a_{0,0} = 2$ ). Isoerror maps computed for stress components are plotted in Fig.  
366 7.

367 Then, based on CSM premises, parametric studies of cavity expansion at normal consolidated  
368 stress state ( $r=1$ ) and highly over-consolidated stress state ( $r=2.9$ ) using ACC2 model are  
369 conducted. It aims at illustrating the advantages brought by the use of this sophisticated model,  
370 when compared to simple models like MCC, for which analytical solutions for the same problem  
371 already exist.

372 (1) ACC2 model with different values of yield shape parameter  $k_f$  (0.5 to 2) as Case 4 and plastic  
373 flow direction parameter  $k_g$  (0.5 to 2) as Case 5 at normally consolidated stress state ( $r_0=1$ ) is  
374 applied to investigate the effect of the shape of yield surface (the yielding behavior) and the shape  
375 of plastic potential surface (the direction of plastic flow).

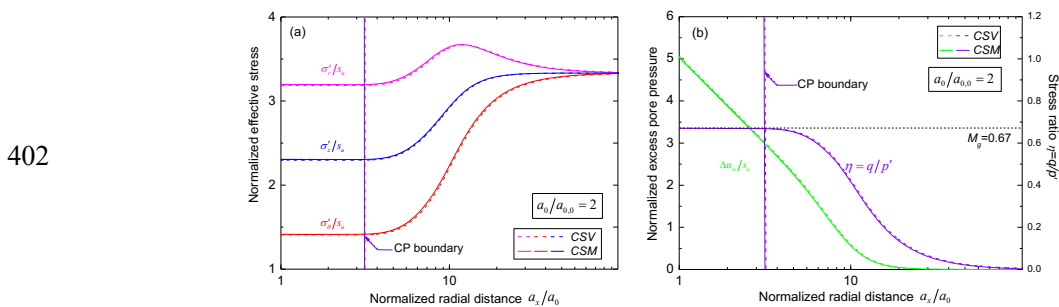
376 (2) ACC2 model with isotropic compression non-linearity parameter  $s$  (4 to 1000) as Case 6 and  
377 deviatoric non-linearity parameter  $A_d$  (0.1 to 5) as Case 7 is applied to investigate the effect of the  
378 nonlinearity at a highly over-consolidated stress state ( $r_0=2.9$ ).

379

380 **4.1 Comparison between CSV and CSM conditions**

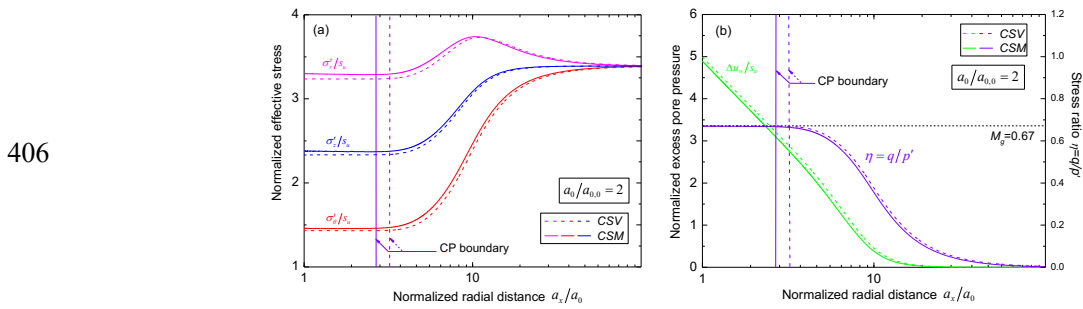
381 The results obtained using CSV and CSM assumptions at three isotropic effective stress states  
 382 ( $p'=2, 10, 50$  MPa) are compared in Fig. 4 as Case 1, Fig. 5 as Case 2 and Fig. 6 as Case 3. The  
 383 soil is initially assumed to be at normally consolidated and isotropic stress state ( $r=1$ ), then rapidly  
 384 expanded to a certain cavity radius ( $a_0/a_{0,0} = 2$ ) without considering the rate and seepage effect.  
 385 During the expanding process, a critical state zone where the stress state at any point satisfies  
 386  $q=M_g p'$  would be formed in vicinity of the cavity. Outside the critical state zone, all material  
 387 points reach the plastic state to some extent.

388 There is a clear difference between CSV and CSM in stress and excess pore pressure  
 389 distributions along the radius distance in Fig. 4-6. From the normalized effective stress ( $\sigma'_r/s_u$ ,  
 390  $\sigma'_\theta/s_u$ ,  $\sigma'_z/s_u$ ) distributions along the radius distance corresponding to the cavity radius ratio of  
 391  $a_0/a_{0,0} = 2$  in Fig. 4(a), Fig. 5(a) and Fig. 6(a), the expanding results obtained based on CSM  
 392 appear to be slightly larger than those based on CSV at each corresponding point. The opposite  
 393 phenomenon could be observed in the normalized excess pore pressure  $\Delta u_w/s_u$  and stress ratio  $\eta$   
 394 distributions along the radius distance in Fig. 4(b), Fig. 5(b) and Fig. 6(b). Meanwhile, the range  
 395 of critical state zone (see CP boundary) for CSM is shorter than for CSV. The CP boundary  
 396 corresponds to the boundary between critical state zone and plastic zone. It can be determined by  
 397 the evolution of current stress ratio ( $\eta=q/p'$ ) along normalized radial distance. With the increase of  
 398 initial isotropic stress, the difference between CSV and CSM becomes more and more obvious.  
 399 Through the comparison between the two cases, it can be concluded that the premise of CSV  
 400 would influence the excess pore pressure and principal effective stress distributions. This confirms  
 401 the necessity of considering the compressibility of pore fluid under high stress conditions.

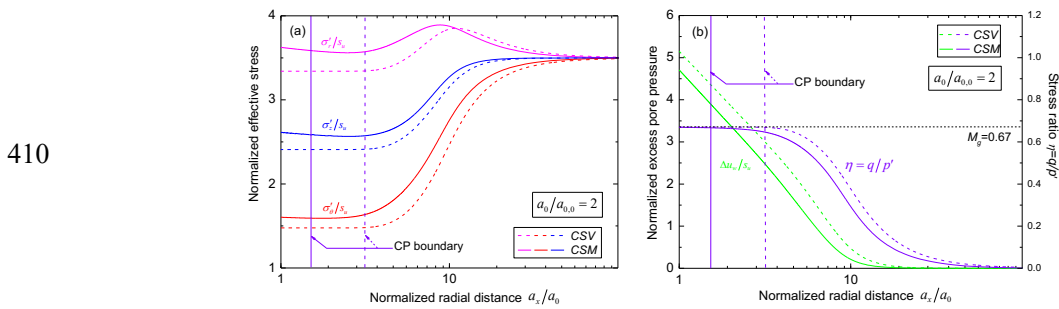


403 Fig. 4 Undrained cavity expansion at normally consolidated and isotropic stress state ( $p'=2$  MPa):

404 (a) normalized principal stress distributions; (b) normalized excess pore pressure and stress ratio  
 405 distribution



407 Fig. 5 Undrained cavity expansion at normally consolidated and isotropic stress state ( $p' = 10$  MPa):  
 408 (a) normalized principal stress distributions; (b) normalized excess pore pressure and stress ratio  
 409 distribution

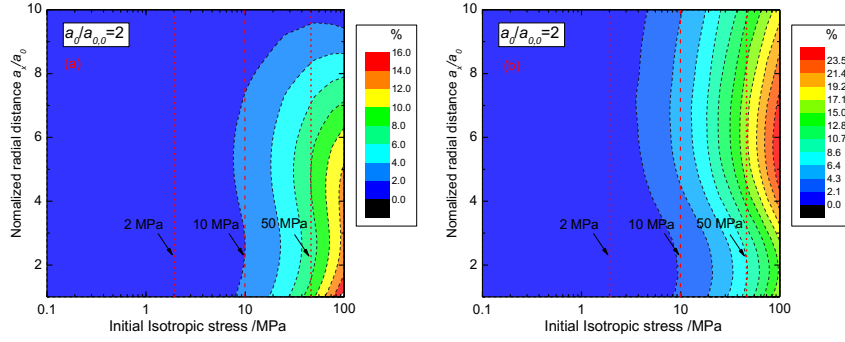


411 Fig. 6 Undrained cavity expansion at normally consolidated and isotropic stress state ( $p' = 50$  MPa):  
 412 (a) normalized principal stress distributions; (b) normalized excess pore pressure and stress ratio  
 413 distribution

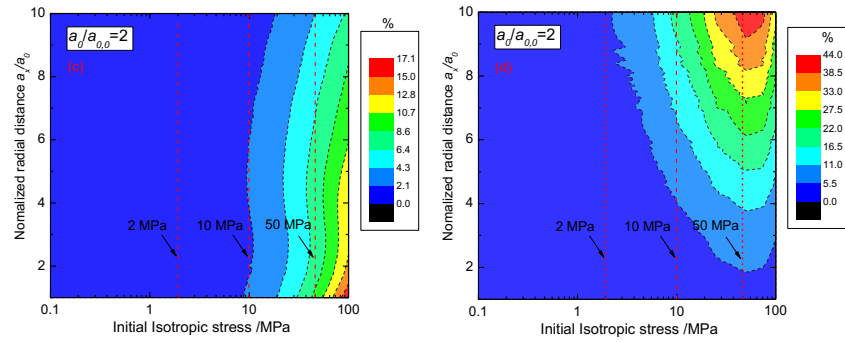
414  
 415 In order to estimate the relative errors based on the two premises, a full range of isotropic  
 416 stress from 0.1 MPa to 100 MPa is considered in cavity expansion process. The relative errors ( $Re$ )  
 417 for three principal stresses and pore pressure are defined as:  $Re = |V_{CSM} - V_{CSV}|/|V_{CSM}|$ . In the  
 418 formula,  $V_{CSM}$ ,  $V_{CSV}$  represent the corresponding results of each material point based on CSM and  
 419 CSV, respectively.

420

421



422



423 Fig. 7 Isoerror maps plotted for constant soil mass (CSM) and constant soil volume (CSV): (a)  
424 radial effective stress; (b) tangential effective stress; (c) vertical effective stress; (d) excess pore  
425 pressure

426 Figs. 7(a)-(c) plot isoerror maps for the three principal effective stress distributions from  $a_x/a_0$   
427 = 1 to  $a_x/a_0 = 10$  in mean effective stress range from 0.1 MPa to 100 MPa when the cavity expands  
428 to  $a_0/a_{0,0} = 2$ . Case 1 of  $p'=2$  MPa, case 2 of  $p'=10$  MPa, case 3 of  $p'=50$  MPa are specially pointed  
429 out. In the range from 0.1 MPa to 1 MPa (low stress conditions), the value of  $Re$  is less than 1%,  
430 suggesting that both cases (CSM, CSV) would get reliable results in principal stress distributions.  
431 However, when the isotropic stress is larger than 10 MPa (relatively high stress conditions), the  
432 value of  $Re$  would increase rapidly. Meanwhile, the  $Re$  value for excess pore pressure distribution  
433 in Fig. 7(d) is much more sensitive to pressure change than the effective stress distribution at both  
434 low and high stress conditions.

435 Thus, for the applications focusing on the evolution of excess pore pressure, CSM would be a  
436 preferential choice for solving the cavity expansion problems even under low stress conditions.

437

438 **4.2 Results with variations of yield surface parameter**

439 A parametric study of cavity expansion is presented as Case 4 with variable  $k_f$  and fixed  $k_g$  ( $k_g =$   
 440 0.9) for  $r=1$  (normally consolidated state) based on CSM. Four different values of  $k_f$  (0.5, 0.7, 0.9,  
 441 2), representing tear shape to elliptical shape, are considered to investigate the impact of the shape  
 442 of yield surface on the stress and pore pressure distributions around the cavity.

443 Fig. 8(a) shows the effective stress paths normalized by the undrained shear strength  $s_u$  from  
 444  $a_0/a_{0,0} = 1$  to  $a_0/a_{0,0} = 2$  at the cavity wall. With the change of  $k_f$  from 0.5 to 2, the shape of yield  
 445 surface varies and the intersection with the critical state line decreases. Figs. 8(b), 8(d) depict the  
 446 normalized effective stresses ( $\sigma'_r/s_u$ ,  $\sigma'_\theta/s_u$ ,  $\sigma'_z/s_u$ ) and pore pressure  $\Delta u_w/s_u$  distributions  
 447 along radius position. The radius position  $a_x$  is normalized by cavity radius  $a_0$  and plotted in the  
 448 scale of logarithm. It can be seen that in the vicinity of cavity wall the three principal stresses  
 449 remain almost unchanged, indicating that the soil in this range has reached the critical state.

450 Further investigation on the shape variation of yield surface shows that positive increment of  
 451  $k_f$  would sharply decrease the values of the three principal stresses in the critical state range (Fig.  
 452 8(a)), but have negligible effects on the location of CP boundary. Fig. 8(c) presents the cylindrical  
 453 cavity expansion curve from  $a_0/a_{0,0} = 1$  to  $a_0/a_{0,0} = 10$  at the cavity wall. The cavity pressure and  
 454 excess pore pressure increase rapidly to a limit and then stay constant with cavity expanding. With  
 455 the change of  $k_f$  from 0.5 to 2, the present solution predicts a decreasing cavity pressure and excess  
 456 pore pressure limit around cavity wall. In Fig. 8(d), the normalized excess pore pressure would  
 457 decrease monotonously along the radial distance. In the vicinity of the cavity wall, the stress point  
 458 would reaches the critical state where three principal stresses ( $\sigma'_r$ ,  $\sigma'_\theta$ ,  $\sigma'_z$ ) remain almost

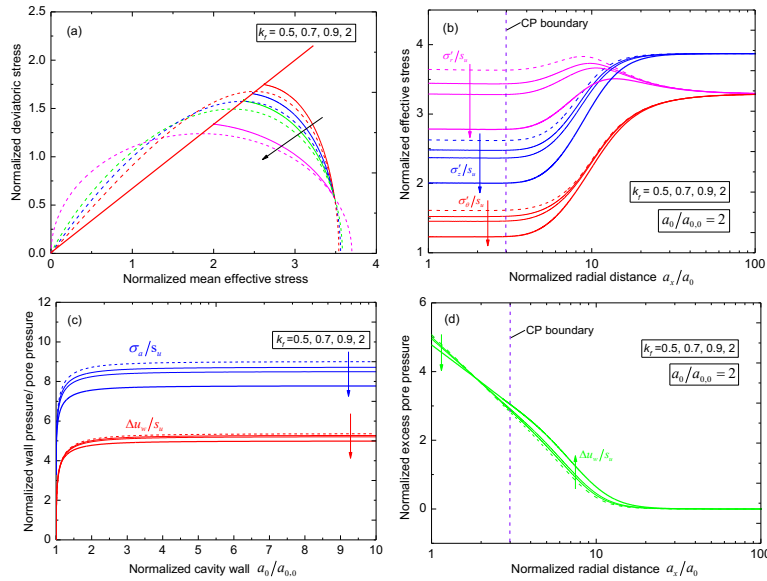
459 constant ( $\frac{d\sigma'_r}{da_x} = \frac{d\sigma'_\theta}{da_x} = \frac{d\sigma'_z}{da_x} = 0$ ) and the radial balance equation ( $\frac{d\sigma'_r}{da_x} + \frac{\sigma'_r - \sigma'_\theta}{a_x} + \frac{du_w}{da_x} = 0$ )

460 would reduce into  $\frac{\sigma'_{rc} - \sigma'_{\theta c}}{a_x} + \frac{du_w}{da_x} = 0$ .  $\sigma'_{rc}$ ,  $\sigma'_{\theta c}$  is the corresponding radial, tangential  
 461 effective stress at the critical state zone, respectively. So the solution of pore water pressure at this  
 462 zone would be  $u_w = -(\sigma'_{rc} - \sigma'_{\theta c}) \ln a_x + C$  ( $C$  is a constant). For the case of cavity expansion,

463  $\sigma'_{rc}$  is larger than  $\sigma'_{\theta c}$  and the excess pore pressure would decrease in the vicinity of the cavity  
 464 wall (critical state zone). Meanwhile, under normal consolidated state, the stress would directly

465 turn into shear contraction state before reaching the critical state line. So the excess pore pressure  
 466 would directly decrease from CP boundary to  $a_x/a_0 = 100$ .

467



468

469 Fig. 8 Undrained cavity expansion results with change of  $k_f$  from 0.5 to 2: (a) normalized stress  
 470 paths at cavity wall; (b) normalized principal stress distributions; (c) normalized cavity expansion  
 471 curve; (d) normalized excess pore pressure distribution

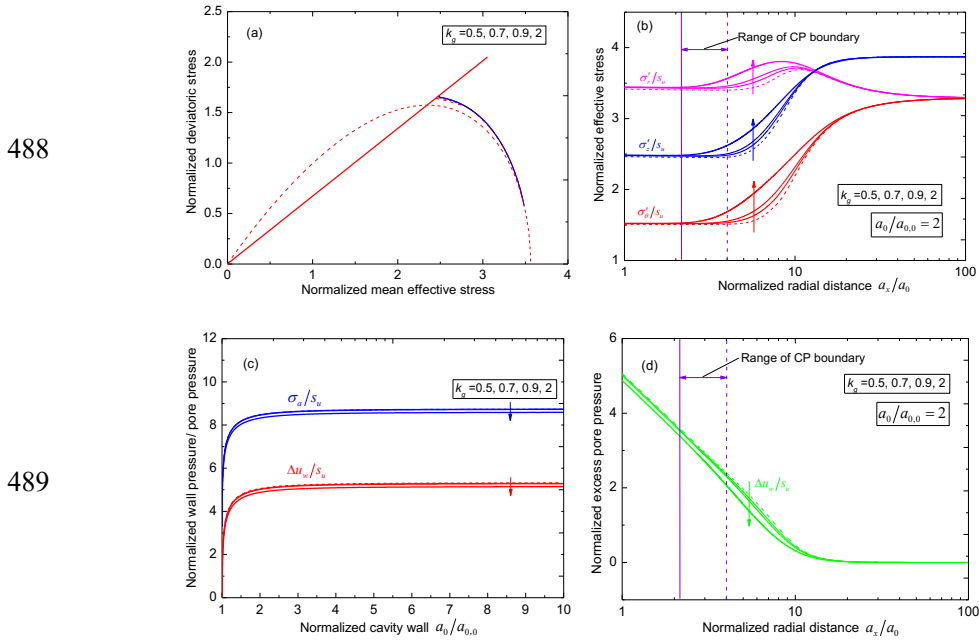
472

### 473 4.3 Results with variations of plastic potential surface parameter

474 A parametric study is presented as Case 5 with variable  $k_g$  and fixed  $k_f$  ( $k_f = 0.7$ ) for  $r=1$  and  $\bar{p}'_c$   
 475 (normally consolidated state) to investigate the impact of the direction of plastic flow on the stress  
 476 and pore pressure distributions around the cavity.

477 From the same initial stress state, the four effective stress paths with different  $k_g$  values (0.5,  
 478 0.7, 0.9, 2) normalized by the undrained shear strength  $s_u$  from  $a_0/a_{0,0} = 1$  to  $a_0/a_{0,0} = 2$  at the  
 479 cavity wall are found to be almost overlapped in Fig. 9(a). This suggests that  $k_g$  merely control the  
 480 direction of plastic flow and portion of shear plastic strain in loading process. Fig. 9(b), 9(d)  
 481 depict the normalized effective stresses ( $\sigma'_r/s_u$ ,  $\sigma'_\theta/s_u$ ,  $\sigma'_z/s_u$ ) and pore pressure  $\Delta u_w/s_u$   
 482 distributions with the variation of  $k_g$ . The effective stresses in the vicinity of cavity wall typically  
 483 remain constant. As opposed to changes of  $k_f$ , the direction variation of plastic flow shows that an  
 484 positive increment of  $k_g$  induces more deviatoric plastic strains, leading to a sharp decrease of the

485 radius of critical state zone, but has negligible effects on the critical values of the three principal  
 486 stresses in the critical state zone. It also shows a slight reduction of excess pore pressure around  
 487 the cavity wall when an increasing plastic shear strain portion is produced.



490 Fig. 9 Undrained cavity expansion results with the variation of  $k_g$  from 0.5 to 2: (a) normalized  
 491 stress paths at cavity wall; (b) normalized principal stress distributions; (c) normalized cavity  
 492 expansion curve; (d) normalized excess pore pressure distribution

493

#### 494 4.4 Results with variations of isotropic nonlinear parameter

495 In highly over-consolidated states, stiff clays typically exhibit a non-linear behavior under loading  
 496 process without pure elastic deformations. A parametric study of cavity expansion in  
 497 over-consolidated states with different isotropic nonlinear parameter  $s$  (4, 8, 20, 1000) is presented  
 498 as Case 6. Note that  $s$  controls the evolution rate of Loading surface in approaching Yield surface,  
 499 namely the nonlinearity of isotropic compression from over-consolidated state to normally  
 500 consolidated state. A smaller  $s$  represents a clear nonlinearity of isotropic loading in  $v$ - $\ln p'$  plane,  
 501 while a larger  $s$  means that the compression line in  $v$ - $\ln p'$  plane is closer to bi-linearity.

502 The expanding cavity is defined by an initial in-situ stress of  $\sigma'_r=1.91$  MPa,  $\sigma'_\theta=1.91$  MPa  
 503 and  $\sigma'_z=2.25$  MPa with a pre-consolidation pressure of  $\bar{p}'_c=6$  MPa and over-consolidation ratio

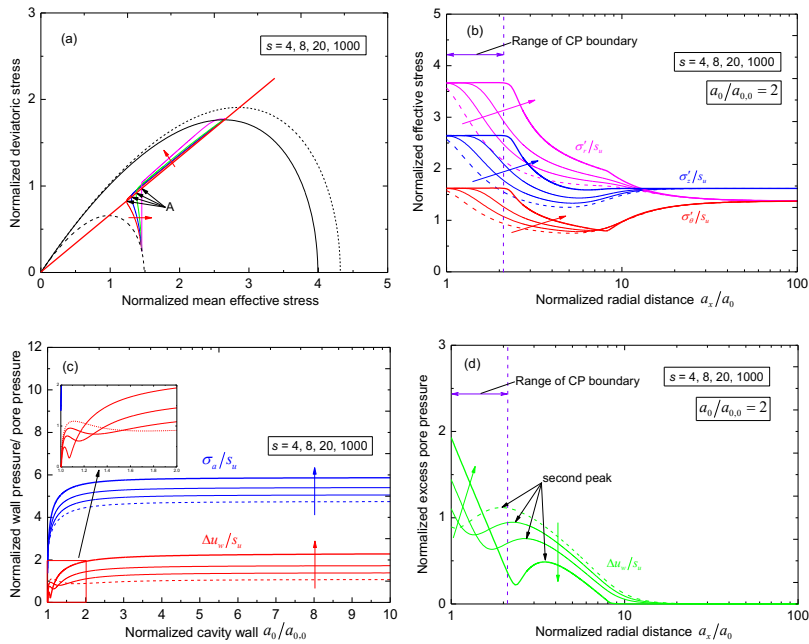
504 of  $r=2.9$  as listed in Table.2. Figs. 10(a)-(d) depict the normalized effective stress paths at cavity  
 505 wall, normalized cavity expansion curves, the normalized effective stresses and excess pore  
 506 pressure distributions with change of  $s$ . Under the expanding process from  $a_0/a_{0,0} = 1$  to  $a_0/a_{0,0} = 2$ ,  
 507 the normalized effective stresses follow different stress paths with  $s$  varying from 4 to 1000 in Fig.  
 508 10(a). The direction of arrow means the increasing trend of  $s$ . When  $s$  reaches the value of 1000,  
 509 the initial mechanical behavior is more elastic which explains the stress path being upward at the  
 510 beginning of undrained loading process.

511 In Fig. 10(b), the range of critical state zone is sharply dependent on  $s$ . But the critical values  
 512 of normalized effective stresses are independent of  $s$ . It is worth noting that with the decreasing of  
 513  $s$  (the increasing nonlinearity of isotropic compression), the radius of critical state zone would  
 514 decrease to zero where no pure critical state zone exists. With the increasing of  $s$  (the decreasing  
 515 nonlinearity of isotropic compression), the radius of critical state zone would increase to a limit  
 516 where no further critical state zone develops. For an extremely large value of  $s$  (e.g. 1000), the  
 517 analytical results are similar to the case of over-consolidated states expressed in modified  
 518 cam-clay model [9]. Meanwhile, the increase in nonlinearity of isotropic compression would  
 519 eventually results in the decrease of effective stress in plastic zone.

520 In Figs. 10(c)-(d), the normalized wall pressure at cavity wall is positive, in agreement with  
 521 the value of  $s$ . A sophisticated phenomenon is observed on the normalized excess pore pressure. At  
 522 the beginning of expanding process, the normalized excess pore pressure would firstly increase,  
 523 decrease and then increase to a limited value. With the increasing of  $s$ , the increasing and  
 524 decreasing phenomenon would be more obvious. At the expanded cavity of  $a_0/a_{0,0} = 2$ , the  
 525 normalized excess pore pressure at cavity wall would increase to a limit value with increasing  $s$ . In  
 526 the critical state zone, the normalized excess pore pressure would decrease along the normalized  
 527 radial distance. Unlike the results by modified cam-clay model [9], a ‘second peak’ of normalized  
 528 excess pore pressure is observed, which is owing to the soil’s shear dilatancy behavior under  
 529 highly over-consolidated states. From  $a_x/a_0 = 100$  to the ‘second peak’, the excess pore pressure  
 530 would increase (shear contraction); from the ‘second peak’ to the CP boundary, the excess pore  
 531 pressure would decrease (shear dilatancy) and the value of excess pore pressure would be  
 532  $-(\sigma'_{rc} - \sigma'_{\theta c}) \ln a_x + C$  ( $C$  is a constant) in the range of critical state zone. The position of the

533 'second peak' is also consistent with the value of  $s$ . In the far end of expanded cavity, excess pore  
 534 pressure would vanish.

535



536

537 Fig. 10 Undrained cavity expansion results with different values of  $s$  from 4 to 1000: (a)  
 538 normalized stress paths at cavity wall; (b) normalized principal stress distributions; (c) normalized  
 539 cavity expansion curve; (d) normalized excess pore pressure distribution

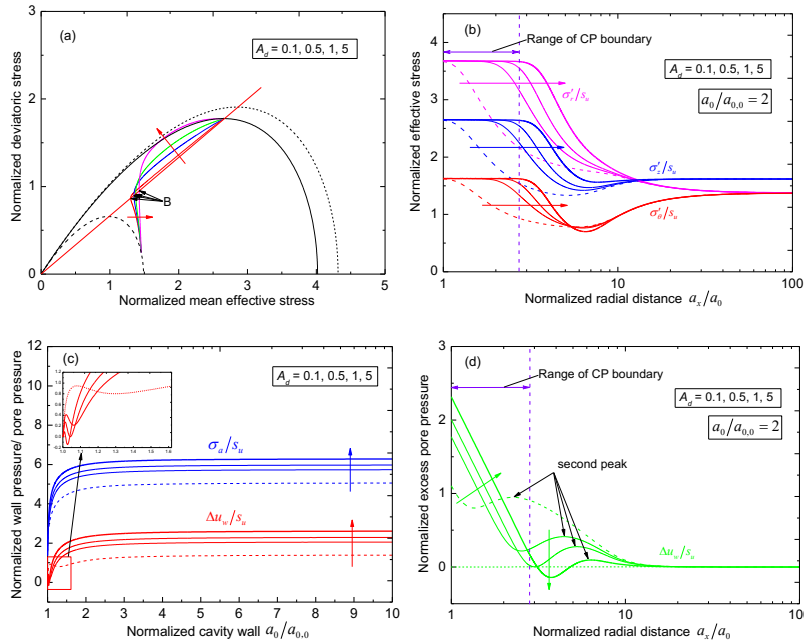
540

#### 541 4.5 Results with the variations of deviatoric nonlinear parameter

542 In over-consolidated states, parameter  $A_d$  describes how the plastic shear strain affects the  
 543 hardening process. It can be calibrated from the stress paths under high over-consolidated states in  
 544 undrained conditions. A parametric study of cavity expansion in over-consolidated states with  
 545 different values of deviatoric nonlinear parameter  $A_d$  (0.1, 0.5, 1, 5) is presented as Case 7.

546 An in-situ stress of  $\sigma'_r=1.91$  MPa,  $\sigma'_\theta=1.91$  MPa and  $\sigma'_z=2.25$  MPa with a  
 547 pre-consolidation pressure of  $\bar{p}'_c=6$  MPa and over-consolidation ratio of  $r=2.9$  is considered to  
 548 evaluate the impact of  $A_d$  on the stress and pore pressure distributions around the cavity.

549



550

551 Fig. 11 Undrained cavity expansion results with different values of  $A_d$  from 0.1 to 5: (a)  
 552 normalized stress paths at cavity wall; (b) normalized principal stress distributions; (c) normalized  
 553 cavity expansion curve; (d) normalized excess pore pressure distribution

554 Figs. 11(a)-(d) depict the results with different  $A_d$  values. Similar to nonlinear parameter  $s$ ,  
 555 the radius of critical state zone is sharply dependent on  $A_d$ . But the critical values of normalized  
 556 effective stress are independent of  $A_d$ . With the decreasing of  $A_d$ , the radius of critical state zone  
 557 would decrease to zero where no pure critical state zone exists. At the expanded cavity of  $a_0/a_{0,0} =$   
 558 2, the normalized excess pore pressure at the cavity wall and the range of critical state zone would  
 559 increase with increasing  $A_d$ . One should also note that the increasing of  $A_d$  means the increasing  
 560 portion of plastic shear strain and the decreasing portion of plastic volumetric strain in hardening  
 561 process. With the increasing of  $A_d$ , the stress path would be more likely upward at the beginning of  
 562 undrained loading process. In Fig. 11(d), a 'second peak' of normalized excess pore pressure is  
 563 also observed and the peak gradually vanish with the increasing of  $A_d$ .

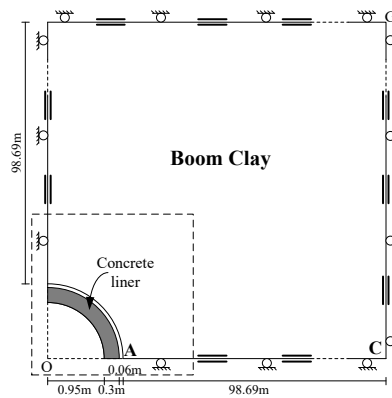
564

## 565 5. Application to Praclay Gallery excavation

566 This section examines the application of the present solution into the excavation of Praclay  
 567 Gallery in underground research facility HADES-URF built at a depth of 223m in natural Boom

568 clay and located in Mol, Belgium [26, 27]. The natural Boom clay is a deposit of  
 569 over-consolidated stiff clay which have been specifically investigated in the previous studies [16].  
 570 Meanwhile, the natural Boom clay is initially considered as homogeneous, at an isotropic effective  
 571 stress of 2.3 MPa and fully saturated with an initial pore pressure of 2.2 MPa.

572 Praclay Gallery is excavated 45 meters long in horizontal plane, so it is regarded as a plane  
 573 strain problem as plotted in Fig. 12. The inner radius of Praclay Gallery and the thickness of the  
 574 concrete liner is equal to 0.95 m, 0.3m, respectively. During the construction of Praclay Gallery, a  
 575 total over-excavation of 0.06m is applied. Since it is finished in a short period (less than 1 day)  
 576 and the intrinsic permeability of natural Boom clay is extremely low ( $2\sim4\times 10^{-19} \text{ m}^2$ ), the  
 577 excavation of Praclay Gallery can also be regarded as an undrained cavity contraction process.



578

579 Fig. 12 Excavation plane of Praclay Gallery in natural Boom clay

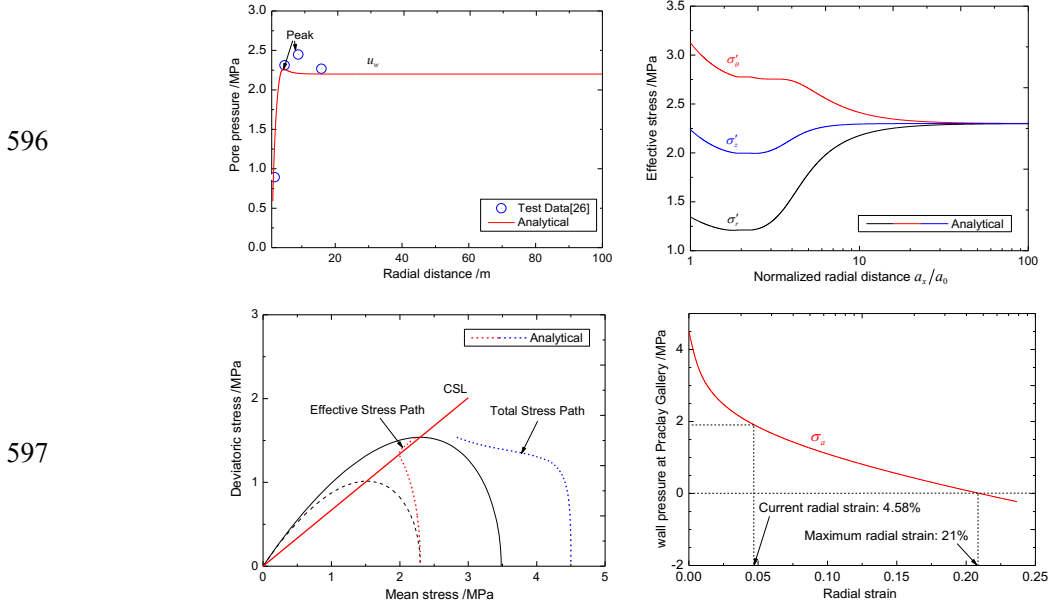
580

581 Fig. 13(a) presents the analytical results by cavity contraction and the test values from four  
 582 pore pressure transducers placed at different nominal radial distances from the center of Praclay  
 583 Gallery [26]. It shows that the present solution could basically describe the pore pressure  
 584 distribution along radial distances. In the vicinity of cavity wall, pore pressure would reduce with  
 585 radial distance decreasing. Then a peak value shows up around the radial distance of 5~10m. After  
 586 that peak, the pore pressure would gradually reduce to its normal value of 2.2 MPa.

587 Fig. 13(b) depicts three principal stress distributions along radial distance by the solution of  
 588 cavity contraction. It shows that the vicinity of cavity wall has not reached the critical state yet.  
 589 The effective stress path of point A in Fig. 13(c) can also be preferential for studying the stress  
 590 states around the contracting wall.

591 In the cavity contraction curve (Fig. 13(d)), the wall pressure at Praclay Gallery would

592 gradually reduce with the increasing radial strain. In the present case, the radial strain is equal to  
 593 4.58% (radial displacement is 0.06m) and a wall pressure of 1.93 MPa is formed. However, when  
 594 the radial strain reaches 21%, the wall pressure would be zero. It indicates that no more supporting  
 595 pressure needs to be added on the cavity wall.



598 Fig. 13 The excavation of Praclay Gallery: (a) pore pressure distribution along radial distance; (b)  
 599 principal effective stress distributions along normalized radial distance; (c) total and effective  
 600 stress paths of Point A; (d) cavity contraction curve

601

## 602 6. Conclusion

603 This paper presents a semi-analytical solution for undrained cylindrical cavity  
 604 expansion/contraction problems using a two-surface plasticity model, which can well reproduce  
 605 the yielding behaviors, unassociated plastic flowing directions and high nonlinearity of stiff clays.  
 606 To develop the new solution, the premise of constant soil mass based on poromechanics is recalled.  
 607 A set of seven governing differential equations is obtained and solved as an initial boundary value  
 608 problem with an auxiliary independent variable  $\zeta$ . The new solution based on constant soil mass is  
 609 then compared with the one based on constant soil volume, showing its relevance under high  
 610 stress conditions. Then, based on the constant soil mass premise, the variations of yield surface  
 611 parameter, plastic flow direction parameter, isotropic nonlinear parameter and deviatoric nonlinear

612 parameter are investigated in a parametric study focusing on the stress paths, stress and excess  
613 pore pressure distributions and cavity expansion/contraction curves. The results obtained allows  
614 the following conclusion to be drawn:

615 (1) The premise of constant soil mass is important in solving cavity expansion/contraction  
616 problems especially under high stress, low porosity and multi-fluid situations. Indeed, under  
617 relatively low stress conditions (e.g.  $p' < 1$  MPa), the solutions based on constant soil mass and  
618 constant soil volume are found to be similar. However, with the increasing of stress, the  
619 compressibility of pore fluid becomes crucial and the volumetric strain could be no longer  
620 regarded as constant. The premise of constant soil mass become preferential.

621 (2) In normally consolidated states, the shape variation of yield surface ( $k_f$ ) would change the three  
622 principal stresses in critical state zone but have no effect on the range of critical state zone. On the  
623 contrary, the variation of plastic flow direction ( $k_g$ ) would change the range of critical state zone  
624 but have no effect on the three principal stresses in the critical state zone.

625 (3) The high nonlinearity means no pure elastic zones in over-consolidated states. The decreasing  
626 of both nonlinearity parameter  $s$  and  $A_d$  decreases the range of critical state zone even to zero  
627 where no pure critical state zone exists. Meanwhile, a ‘second peak’ value of normalized excess  
628 pore pressure along cavity radius is observed and the peak would gradually approach the cavity  
629 wall with the decreasing of  $s$  and  $A_d$ .

630 (4) The present semi-analytical solution can be directly applied to explore the pore pressure, stress  
631 distributions and wall pressure around the expanding/contracting cavity (e.g. Praclay Gallery  
632 excavation).

633

## 634 **Acknowledgements**

635 The authors wish to acknowledge the support of National Natural Science Foundation of China  
636 (51938005) and the European Commission by the Marie Skłodowska-Curie Actions  
637 HERCULES-Towards Geohazards Resilient Infrastructure Under Changing Climates (H2020-500  
638 MSCA-RISE-2017, 778360)

639

640 **Appendix A**

641 The effective stress and total strain increments are defined with three principal components in a  
642 cylindrical coordinate system:

$$643 \quad \mathbf{d}\boldsymbol{\sigma}' = [d\sigma'_r \quad d\sigma'_\theta \quad d\sigma'_z]^T \quad (\text{A - 1})$$

$$644 \quad \mathbf{d}\boldsymbol{\varepsilon} = [d\varepsilon_r \quad d\varepsilon_\theta \quad d\varepsilon_z]^T \quad (\text{A - 2})$$

645 The total strain increment is split into elastic and plastic parts:

$$646 \quad \mathbf{d}\boldsymbol{\varepsilon} = \mathbf{d}\boldsymbol{\varepsilon}^e + \mathbf{d}\boldsymbol{\varepsilon}^p \quad (\text{A - 3})$$

$$647 \quad \mathbf{d}\boldsymbol{\varepsilon}^e = [d\varepsilon_r^e \quad d\varepsilon_\theta^e \quad d\varepsilon_z^e]^T \quad (\text{A - 4})$$

$$648 \quad \mathbf{d}\boldsymbol{\varepsilon}^p = [d\varepsilon_r^p \quad d\varepsilon_\theta^p \quad d\varepsilon_z^p]^T \quad (\text{A - 5})$$

$$649 \quad \boldsymbol{\alpha} = [a_r \quad a_\theta \quad a_z]^T \quad (\text{A - 6})$$

$$650 \quad a_r = \frac{\partial f_l}{\partial \sigma'_r} = \frac{M_f^2}{3(1-k_f)} \left( \frac{2}{k_f} p'^{\frac{2}{k_f}-1} (rp'_c)^{2-\frac{2}{k_f}} - 2p' \right) + 6(\sigma'_r - p') \quad (\text{A - 7})$$

$$651 \quad a_\theta = \frac{\partial f_l}{\partial \sigma'_\theta} = \frac{M_f^2}{3(1-k_f)} \left( \frac{2}{k_f} p'^{\frac{2}{k_f}-1} (rp'_c)^{2-\frac{2}{k_f}} - 2p' \right) + 6(\sigma'_\theta - p') \quad (\text{A - 8})$$

$$652 \quad a_z = \frac{\partial f_l}{\partial \sigma'_z} = \frac{M_f^2}{3(1-k_f)} \left( \frac{2}{k_f} p'^{\frac{2}{k_f}-1} (rp'_c)^{2-\frac{2}{k_f}} - 2p' \right) + 6(\sigma'_z - p') \quad (\text{A - 9})$$

$$653 \quad \mathbf{b} = [b_r \quad b_\theta \quad b_z]^T \quad (\text{A - 10})$$

$$654 \quad b_r = \left( \frac{\partial g}{\partial p'} / \frac{\partial g}{\partial q} \times \frac{\partial p'}{\partial \sigma'_r} + \frac{\partial q}{\partial \sigma'_r} \right) \times k_g \eta = \frac{1}{3} (M_g^2 - \eta^2) + \frac{3}{q} k_g \eta (\sigma'_r - p') \quad (\text{A - 11})$$

$$655 \quad b_\theta = \left( \frac{\partial g}{\partial p'} / \frac{\partial g}{\partial q} \times \frac{\partial p'}{\partial \sigma'_\theta} + \frac{\partial q}{\partial \sigma'_\theta} \right) \times k_g \eta = \frac{1}{3} (M_g^2 - \eta^2) + \frac{3}{q} k_g \eta (\sigma'_\theta - p') \quad (\text{A - 12})$$

$$656 \quad b_z = \left( \frac{\partial g}{\partial p'} / \frac{\partial g}{\partial q} \times \frac{\partial p'}{\partial \sigma'_z} + \frac{\partial q}{\partial \sigma'_z} \right) \times k_g \eta = \frac{1}{3} (M_g^2 - \eta^2) + \frac{3}{q} k_g \eta (\sigma'_z - p') \quad (\text{A - 13})$$

$$657 \quad h = -\frac{\partial f}{\partial p'_c} \frac{\partial p'_c}{\partial \varepsilon_v^p} \frac{\partial g}{\partial p'} - \frac{\partial f}{\partial r} \left( \frac{\partial r}{\partial \varepsilon_v^p} \frac{\partial g}{\partial p'} + \frac{\partial r}{\partial \varepsilon_s^p} \frac{\partial g}{\partial q} \right) \quad (\text{A - 14})$$

$$= \frac{\partial f}{\partial p'_c} \frac{v_0}{\lambda - \kappa} (M_g^2 - \eta^2) + \frac{\partial f}{\partial r} \frac{v_0}{\lambda - \kappa} s(1-r) \left( (M_g^2 - \eta^2) + A_d k_g \eta \right)$$

$$658 \quad \frac{\partial f}{\partial p'_c} = \frac{M_f^2}{1-k_f} p'^{\frac{2}{k_f}} \left(2 - \frac{2}{k_f}\right) p_c^{1-\frac{2}{k_f}} r^{2-\frac{2}{k_f}} \quad (\text{A - 15})$$

$$659 \quad \frac{\partial f}{\partial r} = \frac{M_f^2}{1-k_f} p'^{\frac{2}{k_f}} \left(2 - \frac{2}{k_f}\right) r^{1-\frac{2}{k_f}} p_c^{2-\frac{2}{k_f}} \quad (\text{A - 16})$$

$$660 \quad d\boldsymbol{\sigma}' = \mathbf{D}_{ep} d\boldsymbol{\varepsilon} = \left( \mathbf{D}_e - \frac{\mathbf{D}_e \mathbf{b} \boldsymbol{\alpha}^T \mathbf{D}_e}{\boldsymbol{\alpha}^T \mathbf{D}_e \mathbf{b} + h} \right) d\boldsymbol{\varepsilon} \quad (\text{A - 17})$$

$$661 \quad \mathbf{D}_e = \frac{3K}{1+\nu} \begin{bmatrix} 1-\nu & \nu & \nu \\ \nu & 1-\nu & \nu \\ \nu & \nu & 1-\nu \end{bmatrix} \quad (\text{A - 18})$$

662

663

664

665

666

667

668

669

670

671

672

673

674

675

676 **Appendix B**

677 In the constant soil volume assumption where pore water is regarded as an incompressible fluid,  
 678 the undrained cylindrical cavity expansion/contraction problem is a simple plane strain  
 679 deformation problem with five first-order ordinary differential equations for all material points,  
 680 namely:

$$681 \quad \frac{D\sigma'_r}{Da_x} = \frac{c_{rr} - c_{r\theta}}{a_x} \quad (\text{B - 1})$$

$$682 \quad \frac{D\sigma'_\theta}{Da_x} = \frac{c_{\theta r} - c_{\theta\theta}}{a_x} \quad (\text{B - 2})$$

$$683 \quad \frac{D\sigma'_z}{Da_x} = \frac{c_{zr} - c_{z\theta}}{a_x} \quad (\text{B - 3})$$

$$684 \quad \frac{Dp'_c}{Da_x} = -\frac{\kappa p'_c}{\lambda - \kappa} \frac{c_{rr} + c_{\theta r} + c_{zr} - c_{r\theta} - c_{\theta\theta} - c_{z\theta}}{a_x (\sigma'_r + \sigma'_\theta + \sigma'_z)} \quad (\text{B - 4})$$

$$685 \quad \frac{Dr}{Da_x} = -\frac{\kappa}{\lambda - \kappa} s(1-r) \left( 1 + \frac{A_d k_g \eta}{M_g^2 - \eta^2} \right) \frac{c_{rr} + c_{\theta r} + c_{zr} - c_{r\theta} - c_{\theta\theta} - c_{z\theta}}{a_x (\sigma'_r + \sigma'_\theta + \sigma'_z)} \quad (\text{B - 5})$$

686 where  $D/Da_x$  denotes the material derivative taken along the particle motion path (Lagrangian  
 687 description), and  $\eta$  denotes the current stress ratio  $q/p'$ .

688 Meanwhile, the constant soil volume assumption would induce a constraint following the equation  
 689 regarding the current position of any material point  $a_x$  and the expanded cavity radius  $a_0$ :

$$690 \quad a_x^2 - a_{x0}^2 = a_0^2 - a_{00}^2 \quad (\text{B - 6})$$

691 where  $a_{x0}$  is the initial position of the material point and  $a_{00}$  is the initial cavity radius.

692 The distribution of pore water pressure  $u_w(a_x)$  can be obtained by integrating the radial equilibrium  
 693 equation:

$$694 \quad u_w(a_x) = \sigma'_{r0} + u_{w0} - \sigma'_r(a_x) - \int_{\infty}^{a_x} \frac{\sigma'_r - \sigma'_\theta}{a_x} da_x \quad (\text{B - 7})$$

695

696

697

698 **Appendix C**

699 In isotropic stress state, the total mean stress change ( $dp$ ) and lagrangian porosity change ( $d\phi$ )

700 can be expressed by changes of volumetric strain ( $d\varepsilon_v$ ) and pore water pressure ( $du_w$ ), as follows:

701 
$$dp = \frac{I}{C_d} d\varepsilon_v + b du_w \quad (C - 1)$$

702 
$$d\phi = -bd\varepsilon_v - \frac{I}{N} du_w \quad (C - 2)$$

703 with the Maxwell's symmetry condition given by:

704 
$$b = \left( \frac{\partial p}{\partial u_w} \right)_{\varepsilon_v} = - \left( \frac{\partial \phi}{\partial \varepsilon_v} \right)_{u_w} \quad (C - 3)$$

705 The volumetric compressibility of soil skeleton  $C_d$ , the Biot coefficient  $b$  appearing in Eq (C - 1)

706 are defined as:

707 
$$\frac{I}{C_d} = \left( \frac{\partial p}{\partial \varepsilon_v} \right)_{u_w}, \quad b = \left( \frac{\partial p}{\partial u_w} \right)_{\varepsilon_v} \quad (C - 4)$$

708 The Biot coefficient  $b$ , Biot modulus  $N$  appearing in Eq (C - 2) are defined as:

709 
$$b = - \left( \frac{\partial \phi}{\partial \varepsilon_v} \right)_{u_w}, \quad \frac{I}{N} = - \left( \frac{\partial \phi}{\partial u_w} \right)_{\varepsilon_v} \quad (C - 5)$$

710 Eqs (C - 4, C - 5) are partial differential equations and the subscripts indicate that the

711 corresponding variables are kept constant.

712 Considering the relations between the skeleton and mineral solid properties, the compatibility

713 relations can be obtained:

714 
$$b = 1 - \frac{C_s}{C_d}, \quad \frac{I}{N} = (\phi - b)C_s \quad (C - 6)$$

715 where  $C_s$  is the volumetric compressibility coefficient of mineral solid.

716 In a fully saturated porous medium, the current fluid mass ( $m_w$ ) per unit volume can be expressed

717 as:

718 
$$m_w = \rho_w \phi \quad (C - 7)$$

719 Differentiating Eq (C - 7) gives:

720 
$$\frac{dm_w}{\rho_w} = d\phi + \phi \frac{d\rho_w}{\rho_w} \quad (C - 8)$$

721 The change of fluid density reads as follows:

722 
$$\frac{d\rho_w}{\rho_w} = C_w du_w \quad (\text{C - 9})$$

723 where  $C_w$  is the volumetric compressibility of pore fluid.

724 From Eqs (C - 1, C - 2, C - 6, C - 8, C - 9), the following equation can be obtained:

725 
$$\frac{dm_w}{\rho_w} = -(C_d - C_s)dp - ((\phi C_s - \phi C_w) - (C_d - C_s))du_w \quad (\text{C - 10})$$

726 In undrained conditions, the mass of the fluid phase is constant and  $dm_w = 0$  holds. Thus, the  
727 expressions for incremental pore water pressure can be obtained:

728 
$$du_w = \frac{C_d - C_s}{C_d - C_s + \phi(C_w - C_s)} dp = \frac{d\varepsilon_v - C_s dp}{\phi(C_w - C_s)} \quad (\text{C - 11})$$

729 The well-known Skempton coefficient  $B$  which indicates the ratio between pore pressure  
730 increment and total isotropic stress increment is thus given by:

731 
$$B = \frac{C_d - C_s}{C_d - C_s + \phi(C_w - C_s)} \quad (\text{C - 12})$$

732 The compressibility of pore fluid is usually dozens of times that of solid grain. For most clays, the  
733 compressibility of solid grains can be neglected ( $C_s \approx 0$ ). With infinitesimal transformation, Eq (C  
734 - 11) can be written using Eulerian porosity  $n$  and pore fluid's bulk modulus  $k_w$  ( $k_w = 1/C_w$ ).

735 
$$du_w = \frac{d\varepsilon_v - C_s dp}{\phi(C_w - C_s)} \approx \frac{d\varepsilon_v}{nC_w} = \frac{k_w d\varepsilon_v}{n} \quad (\text{C - 13})$$

736

737 **Data availability statement**

738 The data used to support the findings of this study are available from the corresponding author

739 upon reasonable request.

740 **References**

- 741 [1] Vesic A S. Expansion of cavities in infinite soil mass[J]. *Journal of Soil Mechanics &*  
742 *Foundations Div*, 1972, 98(sm3).
- 743 [2] Carter J P, Booker J R, Yeung S. Cavity expansion in frictional cohesive soils[J]. *Géotechnique*,  
744 1986, 36 (3): 349-358.
- 745 [3] Yu H S, Houlsby G T. Finite cavity expansion in dilatant soils: loading analysis[J].  
746 *Géotechnique*, 1991, 41(2): 173-183.
- 747 [4] Yu H S. *Cavity Expansion Methods in Geomechanics*[M]. Dordrecht, the Netherlands: Kluwer  
748 Academic Publishers, 2000.
- 749 [5] Palmer A C, Mitchell R J. Plane-strain expansion of a cylindrical cavity in clay. Stress-strain  
750 behaviour of soils[C]. *Proceedings of the Roscoe memorial symposium*. Foulis, 1971: 588-599.
- 751 [6] Collins I F, Yu H S. Undrained cavity expansions in critical state soils[J]. *International journal*  
752 *for numerical and analytical methods in geomechanics*, 1996, 20(7): 489-516.
- 753 [7] Cao L F, Teh C I, Chang M F. Undrained cavity expansion in modified Cam clay[J].  
754 *Géotechnique*, 2001, 51(4): 323-34.
- 755 [8] Mo P Q, Yu H S. Undrained cavity expansion analysis with a unified state parameter model for  
756 clay and sand[J]. *Géotechnique*, 2017, 67(6): 503-515.
- 757 [9] Chen S L, Abousleiman Y N. Exact undrained elasto-plastic solution for cylindrical cavity  
758 expansion in modified Cam Clay soil[J]. *Géotechnique*, 2012, 62(5): 447.
- 759 [10] Chen S L, Abousleiman Y N. Exact drained solution for cylindrical cavity expansion in  
760 modified Cam Clay soil[J]. *Géotechnique*, 2013, 63(6): 510.
- 761 [11] Chen S L, Abousleiman Y N. Drained and undrained analyses of cylindrical cavity  
762 contractions by Bounding Surface plasticity[J]. *Canadian Geotechnical Journal*, 2016:  
763 cgj-2015-0605.
- 764 [12] Chen H, Li L, Li J, Wang H. Stress transform method to undrained and drained expansion of  
765 a cylindrical cavity in anisotropic modified cam-clay soils[J]. *Computers and Geotechnics*, 2019,  
766 106: 128-142.
- 767 [13] Sivasithamparan N, Castro J. Undrained expansion of a cylindrical cavity in clays with fabric  
768 anisotropy: theoretical solution[J]. *Acta Geotechnica*, 2018, 13(3): 729-746.
- 769 [14] Chen S L, Liu K. Undrained cylindrical cavity expansion in anisotropic critical state soils[J].  
770 *Géotechnique*, 2018, 69(3): 189-202.
- 771 [15] Carter J P, Randolph M F, Wroth C P. Stress and pore pressure changes in clay during and  
772 after the expansion of a cylindrical cavity[J]. *International Journal for Numerical and Analytical*  
773 *Methods in Geomechanics*, 1979, 3(4): 305-322.
- 774 [16] Hong P Y, Pereira J M, Tang A M, Cui Y J. A two-surface plasticity model for stiff clay[J].  
775 *Acta Geotechnica*, 2016, 11(4): 871-885.
- 776 [17] Avgerinos V, Potts D M, Standing J R. The use of kinematic hardening models for predicting  
777 tunnelling-induced ground movements in London clay[J]. *Géotechnique*, 2015, 66(2): 106-120.
- 778 [18] Avgerinos V, Potts D M, Standing J. The use of kinematic hardening models for predicting  
779 tunnelling-induced ground movements in London clay[J]. *Géotechnique*, 2016, 66(2): 106-120.
- 780 [19] McDowell GR, Hau KW. A generalised Modified Cam clay model for clay and sand  
781 incorporating kinematic hardening and bounding surface plasticity. *Granular Matter* 2004;6:11-6.
- 782 [20] Coussy O. *Poromechanics*. John Wiley & Sons Inc, 2004.

- 783 [21] Spang B. Excel add-in for properties of water and steam in SI-units[J]. Water97\_v13. xla.  
784 Hamburg, 2002.
- 785 [22] Barnichon J D. Contribution of the bounding surface plasticity to the simulation of gallery  
786 excavation in plastic clays[J]. Engineering geology, 2002, 64(2-3): 217-231.
- 787 [23] Cui Y J, Le T T, Tang A M, et al. Investigating the time-dependent behaviour of Boom clay  
788 under thermomechanical loading[J]. Géotechnique, 2009, 59(4): 319-329.
- 789 [24] Mohajerani M, Delage P, Sulem J, et al. The thermal volume changes of the  
790 Callovo-Oxfordian claystone[J]. Rock mechanics and rock engineering, 2014, 47(1): 131-142.
- 791 [25] Monfared M, Delage P, Sulem J, et al. A new hollow cylinder triaxial cell to study the  
792 behavior of geo-materials with low permeability[J]. International Journal of Rock Mechanics and  
793 Mining Sciences, 2011, 48(4): 637-649.
- 794 [26] Van Marcke Ph, Li X L, Bastaens W; Verstricht J et al. The design and installation of the  
795 PRACLAY in-situ experiment[R]. Kessel-Lo: Peter De Preter,2013.
- 796 [27] Charlier R, Chambon R, Collin F, Dizier A, Fauriel S, François B, Fokkens J, Garitte B, Gens  
797 A, Gerard P, et al. Timodaz report: Deliverable d13–simulation of lab and in situ tests[R]. 2010.
- 798 [28] Russell A R, Muir Wood D. A comparison of critical state models for sand under conditions  
799 of axial symmetry[J]. Géotechnique, 2010, 60(2): 133-140.
- 800 [29] Russell A R, Khalili N. On the problem of cavity expansion in unsaturated soils[J].  
801 Computational mechanics, 2006, 37(4): 311-330.
- 802 [30] Borja R I, Lin C H, Montáns F J. Cam-Clay plasticity, Part IV: Implicit integration of  
803 anisotropic bounding surface model with nonlinear hyperelasticity and ellipsoidal loading  
804 function[J]. Computer Methods in Applied Mechanics and Engineering, 2001, 190(26–  
805 27):3293-3323.
- 806 [31] Rouainia M, Wood D M. A kinematic hardening constitutive model for natural clays with loss  
807 of structure[J]. Géotechnique, 2000, 50(2):153-164.
- 808 [32] Hong P Y, Pereira J M, Cui Y J, et al. An elastoplastic model with combined isotropic–  
809 kinematic hardening to predict the cyclic behavior of stiff clays[J]. Computers and Geotechnics,  
810 2014, 62(oct.):193-202.
- 811 [33] McTigue, D. F. Thermoelastic response of fluid - saturated porous rock[J]. Journal of  
812 Geophysical Research Atmospheres, 1986, 91(B9):9533-9542.
- 813 [34] Mohajerani M, Delage P, Monfared M, et al. Oedometric compression and swelling  
814 behaviour of the Callovo-Oxfordia, argillite[J]. International Journal of Rock Mechanics &  
815 Mining Sciences, 2011, 48(4):606-615.
- 816 [35] Barnichon J D. Contribution of the bounding surface plasticity to the simulation of gallery  
817 excavation in plastic clays[J]. Engineering Geology, 2002, 64(2-3):217-231.
- 818 [36] Yang J, Yin Z Y, Liu X F, et al. Numerical analysis for the role of soil properties to the load  
819 transfer in clay foundation due to the traffic load of the metro tunnel[J]. Transportation  
820 Geotechnics, 2020, 23:100336.
- 821 [37] Bian X, Hong Z S, Ding J W. Evaluating the effect of soil structure on the ground response  
822 during shield tunnelling in Shanghai soft clay[J]. Tunnelling and Underground Space Technology  
823 incorporating Trenchless Technology Research, 2016, 58(sep.):120-132.
- 824 [38] Avgerinos V, Potts D M, Standing J R. The use of kinematic hardening models for predicting  
825 tunnelling-induced ground movements in London Clay[J]. Géotechnique, 2016, 66(2):1-15.
- 826 [39] González N A, Rouainia M, Arroyo M, et al. Analysis of tunnel excavation in London Clay

827 incorporating soil structure[J]. *Géotechnique*, 2012, 62(12):1095-1109.

828 [40] Levasseur S, Y Malécot, Boulon M, et al. Soil parameter identification using a genetic  
829 algorithm[J]. *International Journal for Numerical & Analytical Methods in Geomechanics*, 2010,  
830 32(2):189-213.

831 [41] Jin Y F, Yin Z Y, Shen S L, et al. A new hybrid real-coded genetic algorithm and its  
832 application to parameters identification of soils[J]. *Inverse Problems in Science & Engineering*,  
833 2016:1-24.

834 [42] Yin Z Y, Jin Y F, Shen S L, et al. An efficient optimization method for identifying parameters  
835 of soft structured clay by an enhanced genetic algorithm and elastic–viscoplastic model[J]. *Acta*  
836 *Geotechnica*, 2016:1-19.

837 [43] Jin Y F, Yin Z Y, Shen S L, et al. Investigation into MOGA for identifying parameters of a  
838 critical-state-based sand model and parameters correlation by factor analysis[J]. *Acta Geotechnica*,  
839 2015, 454(5):1-15.

840 [44] Yin Z Y, Jin Y F, Shen S L, et al. Optimization techniques for identifying soil parameters in  
841 geotechnical engineering: Comparative study and enhancement[J]. *International Journal for*  
842 *Numerical and Analytical Methods in Geomechanics*, 2018, 42(1).

843 [45] Jin Y F, Yin Z Y, Shen S L, et al. Selection of sand models and identification of parameters  
844 using an enhanced genetic algorithm[J]. *International Journal for Numerical and Analytical*  
845 *Methods in Geomechanics*, 2016, 40(8):1219-1240.

846

847

848

849

850

851

852

853

854

855

856

857

858

859

860

861

862

863

864

865

866

867

868

869

870

871 **LIST OF TABLES**

872 Table.1 The selected parameters of ACC2 model for natural Boom clay

873 Table 2. Summary of material properties of natural Boom clay

874

875

876

877

878

879

880

881

882

883

884

885

886

887

888

889

890

891

892

893

894

895

896

897

898

899

900

901

902

903

904

905

906

907

908

909

910

911

Table 1. The selected parameters of ACC2 model for natural Boom clay

$\lambda$	$\kappa$	$\nu$	$\bar{p}'_c$ : MPa	$M_f$	$k_f$
0.18	0.02	0.3	6	0.67	0.7
$M_g$	$k_g$	$r_0$	$s$	$A_d$	
0.67	0.9	-	8	0.1	

Table 2. Summary of material properties of natural Boom clay

Case	OCR	$\sigma'_r$ : MPa	$\sigma'_\theta$ : MPa	$\sigma'_z$ : MPa	$k_f$	$k_g$	$s$	$A_d$	$r_0$	$\bar{p}'_c$ : MPa	$K_0$	$\nu_0$	$s_u$ : MPa
1	1	2	2	2	0.7	0.9	8	0.1	1	2	1	1.76	0.60
2	1	10	10	10	0.7	0.9	8	0.1	1	10	1	1.47	2.95
3	1	50	50	50	0.7	0.9	8	0.1	1	50	1	1.19	14.29
4	1	5.1	5.1	6	*	0.9	8	0.1	1	*	0.85	1.59	1.55
5	1	5.1	5.1	6	0.7	*	8	0.1	1	5.51	0.85	1.59	1.55
6	2.9	1.91	1.91	2.25	0.7	0.9	*	0.1	0.34	6	0.85	1.61	1.39
7	2.9	1.91	1.91	2.25	0.7	0.9	8	*	0.34	6	0.85	1.61	1.39

$\nu_s=1.84$ ,  $M_g=0.67$ , '\*' means different values are taken.